# High temperature superconductivity with giant pressure effect in 3D networks of boron doped ultra-thin carbon nanotubes in the pores of ZSM-5 zeolite

Yibo Wang<sup>1</sup>, Tsin Hei Koo<sup>1</sup>, Runqing Huang<sup>1</sup>, Yat Hei Ng<sup>1</sup>, Timothée Tianyu Lortz<sup>1</sup>, Ting Zhang<sup>1</sup>, Wai Ming Chan<sup>1</sup>, Yuxiao Hou<sup>1</sup>, Jie Pan<sup>1</sup>, Rolf Lortz<sup>2,\*</sup>, Ning Wang<sup>1,\*</sup>, & Ping Sheng<sup>1,3,\*</sup>

#### **Abstract**

We have fabricated three-dimensional (3D) networks of ultrathin carbon nanotubes (CNTs) within the ~5-Angstrom diameter pores of zeolite ZSM-5 crystals using the chemical vapour deposition (CVD) process. The 1D electronic characteristics of ultrathin CNTs are characterized by van Hove singularities in the density of states. Boron doping was strategically employed to tune the Fermi energy near a van Hove singularity, which is supported by extensive ab-initio calculations, while the 3D network structure ensures the formation of a phase-coherent bulk superconducting state under a 1D to 3D crossover. We report characteristic signatures of superconductivity using four complementary experimental methods: magnetization, specific heat, resistivity, and point-contact spectroscopy, all consistently support a critical temperature  $T_c$  at ambient conditions ranging from 220 to 250 K. In particular, point-contact spectroscopy revealed a multigap nature of superconductivity with a large ~30 meV leading gap, in rough agreement with the prediction of the Bardeen-Cooper-Schrieffer (BCS) theory of superconductivity. The differential conductance response displays a particlehole symmetry and is tuneable between the tunnelling and Andreev limits via the transparency of the contact, as uniquely expected for a superconductor. Preliminary experiments also reveal a giant pressure effect which increases the  $T_c$  above the ambient temperature.

#### Main

Since the discovery of superconductivity in 1911 [1], the search for high-temperature superconductivity has been a key area of condensed matter physics [2]. Conventional superconductors are thought to be limited by the 'McMillan limit' [4], which predicts that a BCS superconductor [3] should not exhibit  $T_c$  values above of 40 K. A breakthrough in high-temperature superconductivity occurred in 1986 with the discovery of the cuprate superconductors [5,6]. Cuprates, characterized by their layered copper-oxide planes, have since achieved ambient pressure  $T_c$  values as high as 134 K in HgBa<sub>2</sub>Ca<sub>2</sub>Cu<sub>3</sub>O<sub>x</sub> [7]. Today, it is clear that cuprate superconductivity is unconventional and results from the interaction of strongly correlated electrons within the framework of a doped Mott insulator [8].

Following the cuprates, iron-based superconductors were discovered in 2008 [9]. They include various families such as 1111, 122 and 11-type and have in the bulk form shown  $T_c$  values up to 55 K [10], with monolayer FeSe grown on SrTiO<sub>3</sub> exhibiting  $T_c$  values exceeding 100 K [11]. Iron-based superconductors are notable for their unconventional nature, with co-existing spin density wave states, orbital order, and superconductivity [10].

<sup>&</sup>lt;sup>1</sup>Department of Physics, The Hong Kong University of Science and Technology, Kowloon, Hong Kong, China <sup>2</sup>Université Grenoble Alpes, INSA Toulouse, Université Toulouse Paul Sabatier, CNRS, LNCMI, Grenoble, France.

<sup>&</sup>lt;sup>3</sup>Clare Hall College, Cambridge University, Cambridge, The United Kingdom

<sup>\*</sup>These authors contributed equally to this work and share last authorship

Nickelates recently added a further class of unconventional high temperature superconductors [12]. Signatures of superconductivity have been reported under high pressure e.g. in La<sub>3</sub>Ni<sub>2</sub>O<sub>7</sub> with  $T_c$  values up to 80 K [13] and up to 40 K at ambient pressure in (La,Pr)<sub>3</sub>Ni<sub>2</sub>O<sub>7</sub> films [14].

Another approach to high temperature superconductivity is taking advantage of the light mass of hydrogen atoms. Metallic hydrogen can be formed under very high pressure and has been seen as a possible exception for the 40 K McMillan  $T_c$  limit [15]. Hydrogen-rich compounds have emerged as candidates for high-temperature superconductivity at high pressures [16]. Examples include H<sub>3</sub>S [17] and LaH<sub>10</sub> [18], which have demonstrated  $T_c$  values above 200 K under pressures exceeding 100 GPa. In contrast, some subsequent reports claiming superconductivity near ambient temperature have been found to be wrong [19].

Our research aimed to advance the field of high-temperature superconductivity by engineering materials to optimize key BCS parameters: high Debye temperature, large electronic density of states (EDOS) at the Fermi level, and strong electron-phonon coupling. One-dimensional ultrathin CNTs [20,21] are ideal candidates due to van Hove singularities, which significantly enhance both EDOS and electron-phonon interactions [22]. Combined with the strong covalent carbon bonds and light atomic mass, high phonon frequencies bring the potential to achieve very high superconducting transition temperatures. Various carbon-based superconductors have been identified, including doped C<sub>60</sub> [23], thin CNTs grown in the pores of zeolite templates [24-29], and bundles of double-walled CNTs [30]. Additionally, unconventional superconductivity has been observed in twisted bilayer graphene [31]. A recent preprint suggests room-temperature superconductivity in graphite flakes, pending independent verification [32].

We report the fabrication of 3D networks of *nearly* interconnected ultrathin (2,1) boron-doped CNTs within  $\sim$ 5 Å pores of calcined ZSM-5 zeolite. This design exploits the 1D electronic structure of CNTs and positions the Fermi level near regions of high density of states – such as van Hove singularities – and promotes superconducting phase coherence through integration in a 3D network. The soft phonon modes in ultra-thin CNTs further enhance electron-phonon coupling. After over two decades of optimization, we observe reproducible signatures of high-temperature superconductivity at ambient pressure, with  $T_c$  values between 220 and 250 K, confirmed by four complementary techniques commonly regarded as key experiments in observing superconductivity.

Point contact spectroscopy with varying tunnelling barrier heights reveals a substantial ~30 meV superconducting gap below ~230 K. The point contact spectra could be tuned between the tunnelling limit and the Andreev limit [33] and shows the characteristic particle-hole symmetry, unequivocally indicating superconductivity as its origin. Specific heat indicates a phase transition near 235 K, which broadens under a magnetic field but with no perceptible change in the peak position, resembling the fluctuation-dominated superconducting transition in cuprates. Electrical resistance shows a steep drop below 278 K by almost 2 orders of magnitude, with the resistance approaching a small residual value below ~100 K attributed to empty zeolite regions and grain boundaries. The transition can be tuned to much higher temperature well exceeding ambient temperature by very little pressure in the kbar range with two screws using a handheld screwdriver. DC magnetization measurements reveal a weak yet characteristic Meissner effect with onset temperature between 220 - 250 K, with differences between zero-field-cooled (ZFC) and field-cooled (FC) data.

We believe our comprehensive experimental evidence supports the initial discovery of hightemperature superconductivity. In particular the observation of Andreev reflection, which is unique to the superconductor/normal metal interface, represents unequivocal evidence for superconductivity. The never-before observed magnitude of the leading gap,  $\sim$ 30 meV, is substantiated by the magnetic, specific heat, and electrical transport measurements, all indicating a very high transition temperature that is in the range of 220-250 K. Hence together they represent clear and convincing proof for high  $T_c$  superconductivity in our system. We hope other groups will reproduce and build on these findings – potentially raising the ambient-pressure  $T_c$  by 40–50 K and achieving the long-sought goal of ambient pressure room-temperature superconductivity.

#### Results:

#### **Point-contact spectroscopy**

Point contact spectroscopy is an energy resolved technique that provides information on the superconducting pairing gap and the order parameter symmetry. With our scanning tunnelling probe, we are able to vary the tunnelling barrier height allowing us to tune the contact between the high-transparency Andreev limit and the low-transparency tunnelling limit. The shape of superconducting spectra can be described by the Blonder-Tinkham-Klapwijk (BTK) formalism [40], where the shape in the tunnelling limit is the characteristic gap suppression surrounded by two coherence peak or shoulders, and the Andreev limit results in a plateau within the bias voltage range corresponding to the gap size.

Extended Data Fig. 1 shows examples of 3 different spectra all taken with different contact transparency from the tunnelling limit (lowest curve) to the Andreev limit (upper curve). Superconducting gap features can be seen either as a depression at zero bias or in the form of shoulder or kink-like structures in the range from ~20 - 30 mV bias voltage. The superconducting gap structure is superposed here on a smooth background, which can be modelled in the form of a parabola. The sign of this parabolic background changes between the extreme tunnelling and Andreev limit, but this is unlikely related to superconductivity as it involves very high energy ranges.

In the following we show data where we carefully fitted each dataset with a parabolic background and normalized the data by it. Details of these fits are shown in Extended Data Fig. 2. Note that the exact shape of this fit does not affect the data analysis, as the superconducting features can be well seen in the raw data, but it facilitates the subsequent fitting with the BTK model. Examples of normalized data is shown in Fig. 1a - d for 4 selected temperatures. Each curve at different temperature represents a new contact point on the sample and hence different contact transparency. However, the contact transparency is only one parameter in the BTK model, which can be adjusted to capture the nature of the contact, while the superconducting gap size  $\Delta$  is independent from it, which is the parameter we are interested in. Fig 1e shows data taken over the entire temperature range up to ambient temperature. It is worth noting that, within the resolution limit, the spectra exhibit symmetry about zero bias, reflecting the particle-hole symmetry characteristic of superconductors.

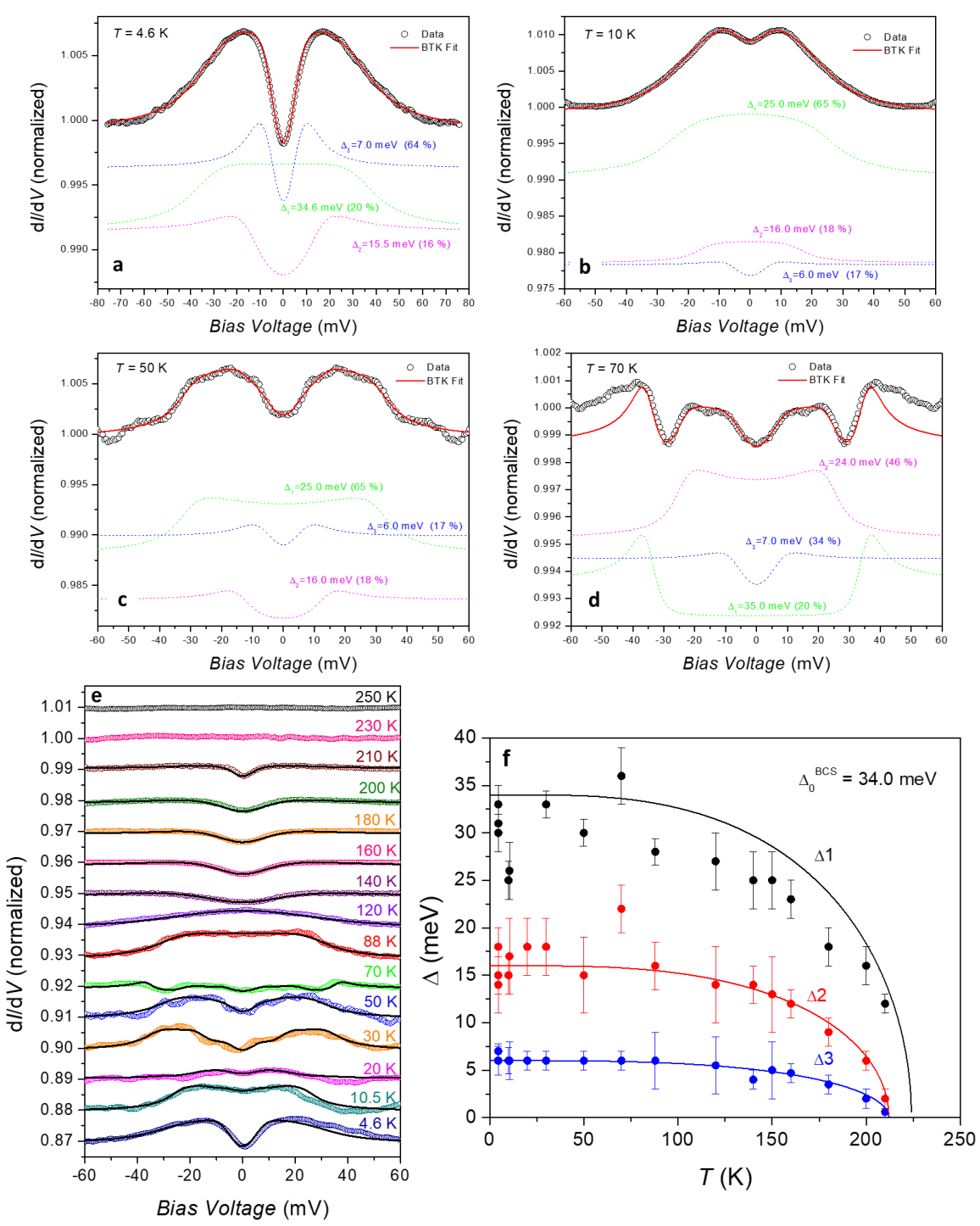


Figure 1 | Temperature dependence of the point contact spectra superconducting gaps in CNT@ZSM-5. a - d, Selected normalized point-contact spectra taken at 4.6 10, 50 and 70 K (circles) with BTK fits (red solid lines). The data has been symmetrized to increase the relative resolution. Additional dashed lines illustrate the individual contributions in our 3-gap-model which are attributed to 3 different bands crossing the Fermi level originating from (2,1) and (3,0) CNTs. e, Temperature dependence of the normalized original point-contact spectra up to 250 K. Offsets of 0.01 have been added, except for the 230 K data. The superconducting gap features vanish above 230 K. b, Temperature dependence of three superconducting gaps from BTK fits. The largest gap closely follows the BCS prediction for  $T_c = 224$  K ( $\Delta_0^{BCS} \approx 34.0$  meV), while smaller gaps show similar trends with lower  $\Delta_0$ . Data scatter reflects variations in contact conditions.

Fitting the curves with a single gap s-wave model fails, which is evident from additional structures in the spectra, which are particularly evident in the 70 K data. It shows a large gap-like depression, but within the depression there is another plateau-like structure with another small depression near zero bias. We obtain good fitting results with a 3-gap s-wave model, which can account perfectly for the experimental data over all the temperature range. The BTK fits are included as solid lines in Fig. 1 a - e, while we added dashed lines in Fig. 1 a - d to illustrate the contributions from the 3 different gaps separately.

In the extreme tunnelling limit, one striking feature is the absence of the so-called coherence peaks, which usually frame the superconducting gap. However, the BTK model can simulate spectra without coherence peaks if the broadening factor associated with the quasiparticle lifetime is large [40]. In our data, the reason for the absence could be either disorder at the sample surface (note that due to the powder nature, our samples have been measured as grown, without any cleaving or cleaning of the surface), or due to a quasi-one-dimensional nature of superconductivity.

For temperatures exceeding 120 K, it became increasingly difficult to distinguish the Andreev reflection contribution from the parabolic background when measured with high transparency contacts, therefore we chose to tune the contact into the low transparency tunnelling limit where the gap depression was clearly visible. For lower temperatures, the high transparency Andreev limit was preferrable as in that limit the distinct features from the 3 gaps were more evident. At 230 K and above the data became perfectly parabolic, irrespective of the contact transparency signalling the absence of coherent superconductivity.

In Fig. 1f we plot the temperature dependence of the fitted gaps. The largest leading gap varies at low temperatures between 25 and 33 meV and then decreases above  $\sim$ 70 K and appears to vanish somewhat below 230 K. The large variation is likely because we needed to re-approach the tip to the sample for each measurement so that slightly different sample positions have been probed. The exact tip pressure may also play a certain role, considering the large pressure dependence of the superconducting transition temperature observed in the resistance measurements. We added the black line, which represents the estimation of the BCS theory for a 224 K superconductor, which corresponds to a gap value  $\Delta_0$  at T = 0 of 34 meV:

$$\Delta(T) \approx 1.76k_BT_c \tanh\left(1.74\sqrt{(\frac{T_c}{T}-1)}\right) = \Delta_0 \tanh\left(1.74\sqrt{(\frac{T_c}{T}-1)}\right)$$
 (1)

This value is slightly larger than the average of our determined values below 20 K, but reasonably close. The low temperature limit of the second gap is 14 – 17 meV, and the smallest gap 6 meV. The two smaller gaps appear to close at slightly lower temperature of 212 K, but within the resolution limit reasonably close to the 224 K temperature determined for the largest gap. This is similar to other known multigap superconductors [41].

In Extended Data Fig. 3 we show point contact data taken at 4.6 K in zero field and in 15 T. Again, the contact needed to be re-adjusted following the field sweep to 15 T, which causes the 15 T data to be more in the Andreev regime than the zero-field data. However, within the resolution limit, the edges of the gap show no significant variation within the experimental resolution, suggesting an extremely high upper critical field far beyond 100 T.

#### Specific heat

The specific heat [35] has been measured for two different batches of samples (#38 and #66) using a few milligrams of sample. Fig. 2a illustrates the total zero-field specific heat divided by temperature (C/T) of CNT@ZSM-5. A tiny second order phase transition anomaly occurs at 236 K superposed on a large phonon background. The small magnitude of this anomaly is anticipated, as in cuprate high-temperature superconductors, the superconducting transition anomaly typically does not exceed 1% of the total specific heat, which at this temperature is predominantly influenced by phonons. Given that the transition temperature coincides with the vanishing of the gap-like features in point contact spectroscopy, we attribute it to the superconducting transition. Fig. 2b shows details of the specific heat near  $T_c$  for both samples. The transition midpoints of the broadened step-like transition differ by about 2.5K in these two samples (Sample 1:  $T_c = 236$  K, Sample 2:  $T_c = 233.5$  K) with the transition of Sample 2 being significantly broader.

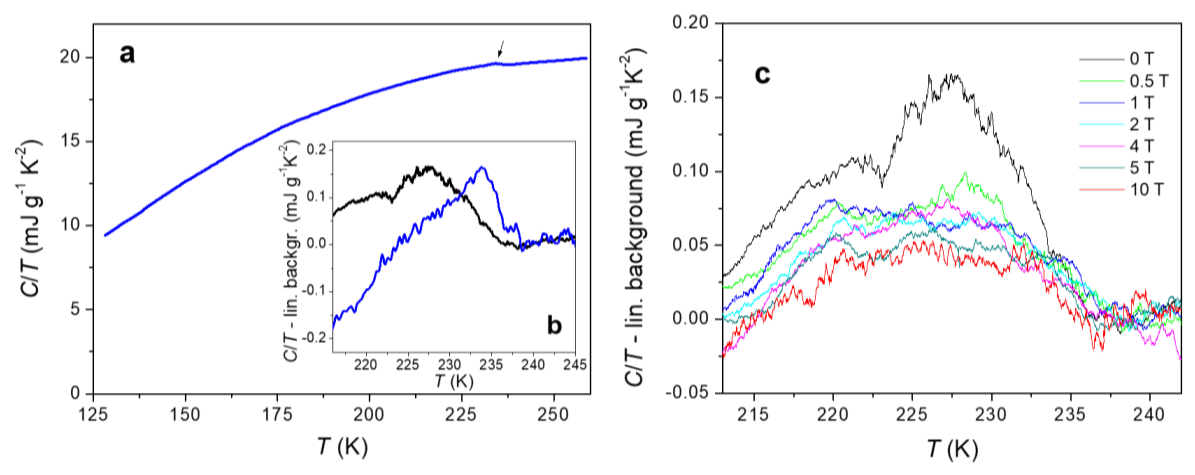


**Figure 2** | **Specific heat of CNT@ZSM-5. a**, The total specific heat divided by temperature C/T in zero field (Sample 1, delineated in blue) shows a small  $2^{nd}$  order phase transition anomaly at 236 K (arrow) attributed to the superconducting transition. **b**, C/T for two different samples (Sample 1: blue, Sample 2: black) reveals slight variations of  $T_c$  and transition width. A linear background fitted above  $T_c$  has been subtracted for clarity. **c**, C/T for Sample 2 under magnetic fields up to 10 T after subtraction of the linear background, showing broadening of the transition due to superconducting fluctuations.

Accurately estimating the phonon contribution to the specific heat is a complex task for high-temperature superconductors, with few approaches available for estimating the electronic specific heat in cuprate superconductors. The even more complex nature of the CNT-zeolite composite makes this challenge even greater, and at such high temperatures almost impossible. Fig. 2c presents C/T data measured in various applied fields up to 10 T, following the subtraction of a simple straight line, which fits well the background of Sample 2 in this small temperature interval. The zero-field data exhibit a small but relatively sharp jump centred at 233.5 K, followed by a broader bump peaking at 228 K. The width of this feature does not allow us to determine whether it represents the typical BCS mean-field type phase transition, characterized by a jump in specific heat, or the diverging lambda transition typical of cuprate superconductors, where 3D-XY phase fluctuations dominate the transition shape [36,37]. The zero-field transition of Sample 1 (Fig. 2b) shows a small upturn below the jump that could indeed indicate a lambda transition.

Under a magnetic field, the anomaly of Sample 2 broadens rapidly, resulting in a broad bump. This behaviour is characteristic of a fluctuation-dominated superconducting transition, commonly observed in cuprates where the field reduces the effective dimensionality of the

superconductor, driving the transition shape towards a continuous crossover [38]. Phase coherence is then established only below a vortex melting transition that occurs at lower temperatures [39]. Our resolution is insufficient to observe the latter, but the overall transition behaviour agrees perfectly with what is known from cuprates. Given the unknow value of the electronic specific heat, which is impossible to extract at such high temperatures without knowing the phonon contribution, it is not possible to extract more detailed information, such as the coupling strength, paring symmetry, superconducting gap value or condensation energy.

#### Electrical resistance

Fig. 3 presents two-probe resistance measurements on approximately 1 mg of CNT@ZSM-5 powder, compressed between two 1.2 mm screws in a polyamide block. While the  $\sim$ 0.1  $\Omega$  resistance of the screws is negligible, contact resistance at the screw-sample and grain interfaces contributes to a small residual resistance. The inset shows the raw resistance data: the black curve was recorded after slightly compressing the powder and then reducing the pressure while maintaining a stable current path. Above 280 K, the resistance varies linearly with temperature, but drops sharply below 276 K, indicating a pronounced transition. Below this point, resistance remains finite and gradually approaches a residual value ( $\sim$ 5 % of the normal state value above  $T_c$ ) near 100 K. In the main panel, this residual resistance has been subtracted, and the data normalized to the normal-state resistance at the transition onset to enable comparison with pressurized measurements.

For the green curve the screws have been tightened with a torque of M=1 Nm using a handheld screwdriver with built-in torque meter, which results in an overall significantly lower resistance (inset). The longitudinal force generated by the screw can be calculated by  $F=2\pi \ v \ M \ / \ s$ , where s=0.25 is the slope of the M1.2 screw and v is the efficiency of the screw connection for which we use a standard value of 0.6. While the generated pressure on the order of  $p\approx 0.1$  kbar is certainly not very hydrostatic due to the lack of a pressure transmitting medium, the fine powder nature of the sample should still lead to quasi-hydrostatic conditions. Surprisingly, the curve (which largely retains its shape) shifts towards higher temperature by more than 100 K with the lower onset of the resistive jump exceeding ambient temperature. This is an enormous pressure dependence. By tightening the screw at ambient temperature before the experiment, we consistently observed a pressure-induced resistance drop, indicating a transition into the ambient-temperature superconducting state. This effect was reproducible across multiple pressure cycles. Extended Data Fig. 4 shows additional data at different pressures.

The residual resistance at ambient pressure below 100 K varied slightly between pressure cycles, remaining around 5% of the normal state resistance above  $T_c$  (see inset of Fig. 3). Extrapolating the steepest slope to zero yields an estimated  $T_c^0$  of 239 K, indicating the onset of phase coherence in the superconductor. This aligns well with superconducting transitions observed in specific heat. Such agreement is expected, as the specific heat transition in fluctuation-dominated samples typically coincides with the macroscopic onset of phase coherence, a prerequisite for zero resistance.

Although zero resistance cannot be directly confirmed due to the 2-probe measurement setup, the pronounced resistance drop – nearly two orders of magnitude – strongly supports the presence of a superconducting transition. This drop spans a relatively broad temperature range, which may be attributed to sample inhomogeneities, pressure gradients from the screw-based setup, or intrinsic fluctuation effects, which are expected to be significant near ambient temperature. Additionally, the observed noise in the data is independent of current magnitude,

indicating it likely arises from mechanical stress and grain movement caused by thermal expansion during cycling.

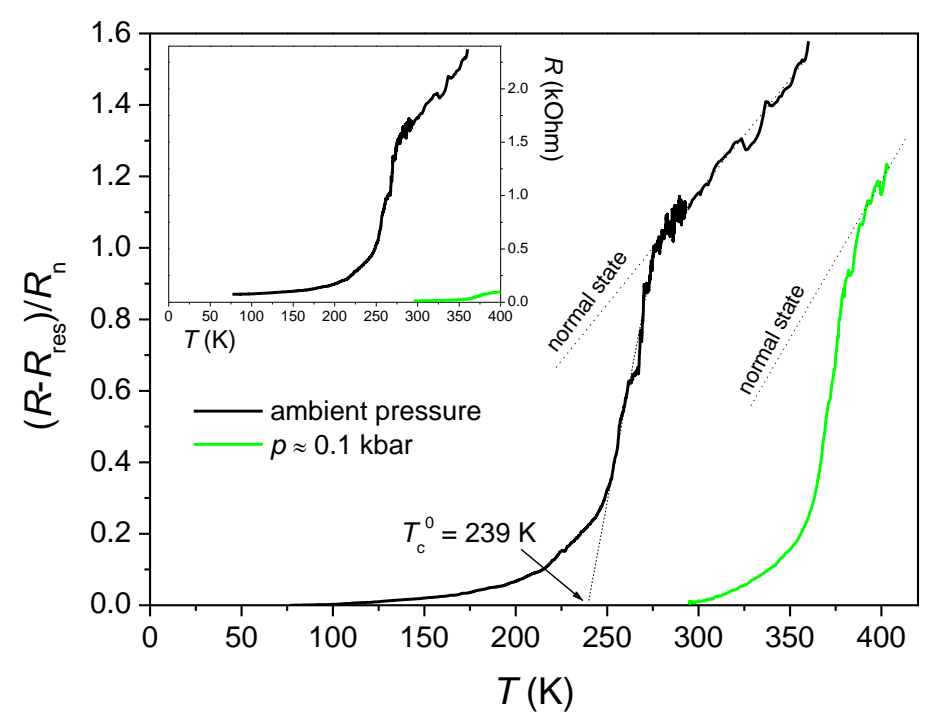


Figure 3 | Electrical resistance of CNT@ZSM-5 powder measured in a two-probe setup using brass screws in a polyamide block. In the main panel, residual contact resistance has been subtracted and data normalized to the normal-state resistance at the transition onset. Black curve: ambient pressure; green curve:  $\sim$ 0.1 kbar applied via 1 Nm torque on M1.2 screw. Dashed lines indicate the linear normal-state behaviour above  $T_c$  and an extrapolated slope yielding  $T_c^0 \approx 239$  K. The inset shows raw resistance data, highlighting a strong pressure-induced shift of  $T_c$  to above ambient temperature.

Data from other batches, including enlarged figures of the resistance raw data are shown in Extended Fig. 5. To enable true four-probe measurements, the device was modified with two screw holes intersecting at 45°, allowing compression from four screws. Despite this, the results remained similar, with a persistent residual resistance (Extended Data Fig. 5b & e). This suggests the residual resistance arises from series conduction paths at grain boundaries or insulating regions within the zeolite matrix. Achieving true zero resistance may require further sample optimization or grain boundary treatment. Nonetheless, the substantial resistance drop, along with the emergence of a gap-like feature and Andreev reflection signals below 230 K in tunnelling experiments, strongly supports a superconducting transition.

#### **DC** magnetization

Fig. 4 presents DC magnetization data under ZFC and FC conditions in magnetic fields of 200 Oe for four different sample batches #61, #62, #66 and #67. To enhance clarity, a weak linear background was subtracted, fitted at the highest temperature (Extended Data Figs. 6 - 8). Below an onset temperature that varies between 220 K and 250 K among the different batches, a negative contribution typical for the superconducting Meissner effect emerges in the ZFC branch, with a separation of the ZFC and FC branches. Further data in different fields is shown in Extended Data Figure 9 & 10.

The onset of a weak diamagnetic signal between 220–250 K, varying by sample batch, provides further evidence for high-temperature superconductivity in CNT@ZSM-5. The signal's weakness is likely due to the powder form, with crystallites smaller than the London penetration depth.

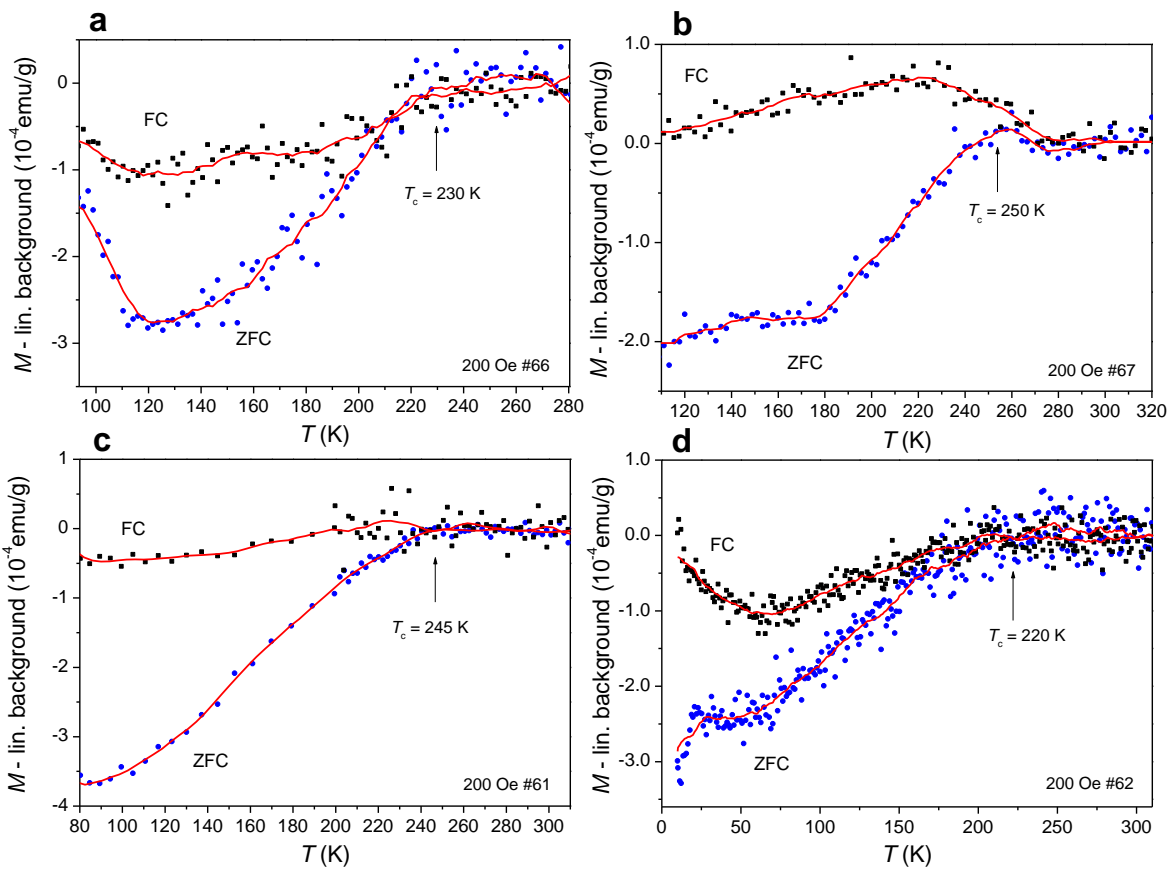


**Figure 4** | **DC magnetization of CNT@ZSM-5.** Examples of DC magnetization data measured under ZFC and FC conditions for four different batches of samples measured in a 200-Oe field. A weak linear background fitted above ~250 K has been subtracted for clarity. An onset of Meissner diamagnetism with difference in the ZFC and FC branches is observed below 220 – 250 K. Symbols represent the measured data, while red lines were generated by adjacent averaging over 5 -10 points to enhance clarity.

#### Discussion

We observed the expected superconducting characteristics in four complementary probes that are commonly used to study superconductivity. These probes cover thermodynamic measurements, including magnetisation and specific heat, as well as electrical transport and energy-resolved point contact spectroscopy experiments. All the observed features clearly resemble those of other superconductors, but at significantly higher temperatures than any known ambient-pressure superconductor. The  $T_c$  variation with the magnetic field is noted to be almost imperceptible up to 15 T.

The magnetisation response was found to be very small. This is probably because the micronsize zeolite crystals are smaller than the London penetration depth. This results in incomplete Meissner screening. Additionally, while the lower critical field ( $H_{c1}$ ) is expected to be small, a larger applied field is required to observe minor magnetisation contributions, which further reduces the Meissner screening effect. The difference between the ZFC and FC branches is evident but varies depending on the sample batch and field strength. Some data show diamagnetic contributions in both branches. In rare cases, the FC curve even shows a positive contribution. This phenomenon is known as the paramagnetic Meissner effect and results from a superconducting surface effect [42]. All ZFC curves demonstrate the Meissner effect, albeit not in the form of a sharp jump, but rather as a continuous kink. This can be attributed to the smallness of the signal, which made it impossible to detect superconductivity in very small fields below  $H_{c1}$ . We had to apply at least 100 Oe to clearly observe superconductivity, which typically results in a continuous transition.

The electrical resistance measurements revealed a two orders of magnitude change, with resistance increasing by from a small, temperature-independent value below ~70 K. By extrapolating the steepest slope of the resistance curve to zero temperature, we obtain a  $T_c^0$  in the range of 239 K, which is consistent with the phase transition observed in specific heat data, the onset of a stronger Meissner effect in magnetization, and the disappearance of gap-like features in tunneling experiments.

Specific heat measurements align well with expectations, suggesting that a significant proportion of the sample exhibits superconductivity. Similar to the behaviour observed in cuprates, the transition appears fluctuation-dominated and the presence of a magnetic field broadens it into a bump-like crossover. In these materials, this effect arises due to the magneticfield induced finite size effect in the presence of fluctuations of the anisotropic 3D-XY universality class [43,44]. The associated length scale, dictated by the vortex separation, prevents the superconducting correlation length from diverging. The difference from the cuprates is that our sample is a 3D network of 1D metallic objects, whereas cuprates have weakly coupled 2D layers. Reduced dimensionality strongly enhances fluctuations in the phase of the superconducting order parameter. In this case, Cooper pairs first form at a high temperature in the 1D nanotubes (or 2D planes of the cuprates), without phase coherence. Then, correlations gradually form until, at  $T_c$ , a phase-coherent superconducting condensate is formed. For cuprates, fluctuations can extend up to twice the  $T_c$  value and can be observed in either thermodynamic quantities [33,34] or as vortex excitations in the Nernst effect [45]. A similar situation is likely here, as magnetisation and specific heat data suggest a  $T_c$  of 220 – 250 K. This corresponds to the temperature at which resistance approaches zero, while the onset of the resistive transition occurs at 278 K, which is well above the melting point of ice. This transition's width corresponds to the range in which Cooper pairs begin to develop correlations until a phase-coherent zero-resistance state is formed. It should be noted that Cooper pairs may exist at an even higher temperature in the form of pre-formed pairs [46,47], but without correlations. It would be interesting to investigate the possible presence of a pseudogap phase using true tunnelling experiments, but this is beyond the capabilities of our point contact setup.

Among the probes used, point contact spectroscopy provided further convincing evidence of superconductivity. The symmetry of the spectra demonstrates a clear particle-hole symmetry, a characteristic feature of superconductors. Achieving the Andreev limit further confirms the superconducting origin of the measured effects. Three distinct superconducting gaps were identified. To understand the origin of the multiple gaps, we performed ab initio band structure calculations. Extended Data Fig. 11 shows the electronic band structure of (2,1) and (3,0) CNTs, confirming their metallic nature. The existence of two types of CNTs is revealed by the Raman signals in comparison to the ab initio calculations, discussed in the Methods section. It is also consistent with the geometric constraint presented by the two sets of pore channels in ZSM-5. Ab initio calculations also indicate that boron doping shifts the Fermi level down by  $\sim 0.5$  eV. This places it in direct vicinity of a van Hove singularity for (2,1) CNTs (see Extended Data Fig. 11). This supports the idea of inducing phonon-mediated high- $T_c$  superconductivity. We believe that (2,1) CNTs are the leading cause of superconductivity. The Fermi level crosses three bands, which are likely responsible for the three superconducting gaps observed. The (3,0)

CNTs may also contribute to superconductivity via the proximity effect. Despite the significant scatter in the measured gap values, which resulted from the necessary adjustments to the tip after each temperature variation, the obtained data remains consistent with BCS theory expectations for a superconductor with a  $T_{\rm c}$  near 224 K. However, within the limits of the relatively large error bars, the temperature dependence of the gaps appears to decrease more continuously and linearly than strictly following the BCS trend.

Our findings reveal no significant magnetic field dependence apart from the broadening of the specific heat transition. This suggests an extremely high critical field, well beyond 100 T, and indicates that the material exhibits robust superconducting properties even under very strong magnetic fields. This is not unexpected, given that other known high- $T_c$  superconductors, such as the cuprates and Fe-based superconductors have upper critical fields well beyond 100 T.

One of the most striking observations is the dramatic pressure effect on  $T_c$ . The substantial  $T_c$  increase in resistance measurements, to values exceeding room temperature is highly unusual:  $\sim 0.1$  kbar increases  $T_c$  by  $\sim 100$  K! Although our experiment was not planned as a high-pressure experiment with non-ideal conditions, the significant  $T_c$  increase, where ambient temperature superconductivity can be induced by simply turning a small screw with a handheld screwdriver, is remarkable. Further pressure experiments under better hydrostatic conditions with precise pressure determination are desirable to investigate this pressure dependence more quantitatively.

The strong pressure dependence may stem from the vicinity of the van Hove singularity to the Fermi level; pressure is likely to shift the associated flat band, enhancing the density of states at the Fermi level - a key factor for high  $T_c$  per the McMillan formula [4]. Additionally, the soft zeolite matrix may deform CNTs under pressure, altering phonon modes and influencing  $T_c$  in a phonon-mediated mechanism. Note that the (2,1) CNTs are extremely instable and are only stabilized by the confinement in the zeolite matrix as indicated by imaginary phonon frequencies in the phonon density of states (Extended Fig. 11). This, together with the vicinity of a van Hove singularity makes these (2,1) CNTs an extremely exotic metallic material. However, our current data do not allow us to determine the pairing origin.

Our interconnected network of CNTs has a unique feature that could further explain the strong pressure effect. The perpendicular CNTs are separated by a small 1.3 Å gap (see Fig. 5 in the Methods section) and do not intersect. At such small separation, some bonding may be inevitable. However, such intersections would be the mechanically weak points in the system. Due to the soft crystal lattice of ZSM-5 zeolite, pressure deforms the zeolite, thereby pushing the perpendicular CNTs closer together until they eventually touch. This leads to a dimensional crossover between 1D and 3D. As previously discussed, phase-incoherent, preformed Cooper pairs may exist well above  $T_c$ , the temperature at which they condense into a phase-coherent condensate. When the CNTs approach at their perpendicular intersections, the resulting 3D network will suppress fluctuations and establish a phase-coherent superconducting state at a higher temperature. Further experiments to confirm the existence of phase-incoherent pairing above  $T_c$  are desirable, including more sensitive tunnelling experiments and measurements of the thermoelectric Nernst effect [45].

In theory, the mathematical solution of the Ginzburg-Landau equation in the network geometry, either analytically or numerically, may offer some insights to the present nanostructured system.

#### **Concluding remarks**

Our study reveals a new high-temperature superconductor with an ambient-pressure  $T_c$  between 220–250 K and a resistive onset as high as 278 K – above 0 °C – which can be significantly

enhanced by applying minimal pressure. Despite these promising results, challenges remain. The insulating zeolite host and grain boundaries contribute to residual resistance, and the small crystallite size limits the Meissner effect in magnetization measurements. These findings highlight the need for improved sample preparation, such as using larger zeolite crystals and surface treatments to reduce grain boundary effects. Nonetheless, the reproducibility of the transition and supporting tunneling data strongly suggest superconductivity.

We hope that our discovery will stimulate similar efforts within the research community, as has been seen with other known high- $T_c$  superconductors, leading to a new understanding of strongly correlated electronic phases. Although developing the material took us over two decades, preparing it is not particularly complicated, with the elemental carbon responsible for its superconductivity being one of the most common elements in the universe.

#### Methods

#### Sample fabrication and characterization

ZSM-5 zeolite, a microporous aluminosilicate with a three-dimensional interconnected pore network, served as the template for synthesizing single-walled carbon nanotubes (SWCNTs). Its pore structure comprises straight channels (5.4 × 5.6 Angstrom diameter along the b-axis) and slightly undulating channels (5.1 × 5.5 Å slightly elliptical cross section along the a-axis), as illustrated in Fig. 5a. The typical size of a ZSM-5 zeolite crystallite ranges from 3 to 4 microns (Fig. 5b). Channels in ZSM-5 form a 3D network with ~1 nm lattice constant. However, it should be noted in Fig. 5c&d that the perpendicular channels do not directly cross. Rather, they are separated by ~1.5 Angstroms vertical distance at the point of closest approach, see inset to Fig. 5e. These sub-nanometer channels restrict nanotube growth to a diameter below 0.3 nm. The somewhat different geometric cross sections of the channels along the a and b axes have a direct consequence on the type of ultra-thin CNTs being formed in each channel type.

Prior to synthesis, commercial ZSM-5 crystals were calcined at 550°C for 6 hours in air to remove organic residues and adsorbed water, ensuring clean pore channels. Boron-doped carbon nanotube networks were synthesized in ZSM-5 via a CVD process. The calcined zeolite was loaded into a quartz boat, degassed at 200°C under vacuum (10<sup>-3</sup> mbar) for 2 hours, and then heated to 910°C at 24°C/min. At 910 °C, the in situ-generated diborane and hydrogen gas (B<sub>2</sub>H<sub>6</sub> and H<sub>2</sub>, 62 cm<sup>3</sup>, 1.4 atm) and high-purity methane (99.99%, 200 sccm, at 6 atm) were sequentially released into the CVD chamber (200 cm<sup>3</sup>) and co-flowed through the zeolite bed in a setup shown in Fig. 6. Diborane was synthesized via the reaction of small amounts of iodine and sodium borohydride ( $I_2 + 2NaBH_4 \rightarrow 2NaI + B_2H_6 + H_2$ ) at 180°C for 2 hours in a sealed vessel that was used as the boron source. The total system pressure was maintained at 6 atm for 5 hours using a MKS651C controller. Due to imperfect sealing of the CVD chamber, there was some residual methane flow, necessary to maintain the constant pressure. Such residual methane flow inevitably caused a gradual decrease in boron concentration, necessitating re-introduction of diborane after 3 hours to maintain doping uniformity over time. After 5 hours, methane source was closed, and the chamber was evacuated. Controlled cooling to 750°C (1°C/min) was carried out to facilitate surface carbon sublimation as well as sample annealing. Oven was turned off after that to allow natural cooling to room temperature.

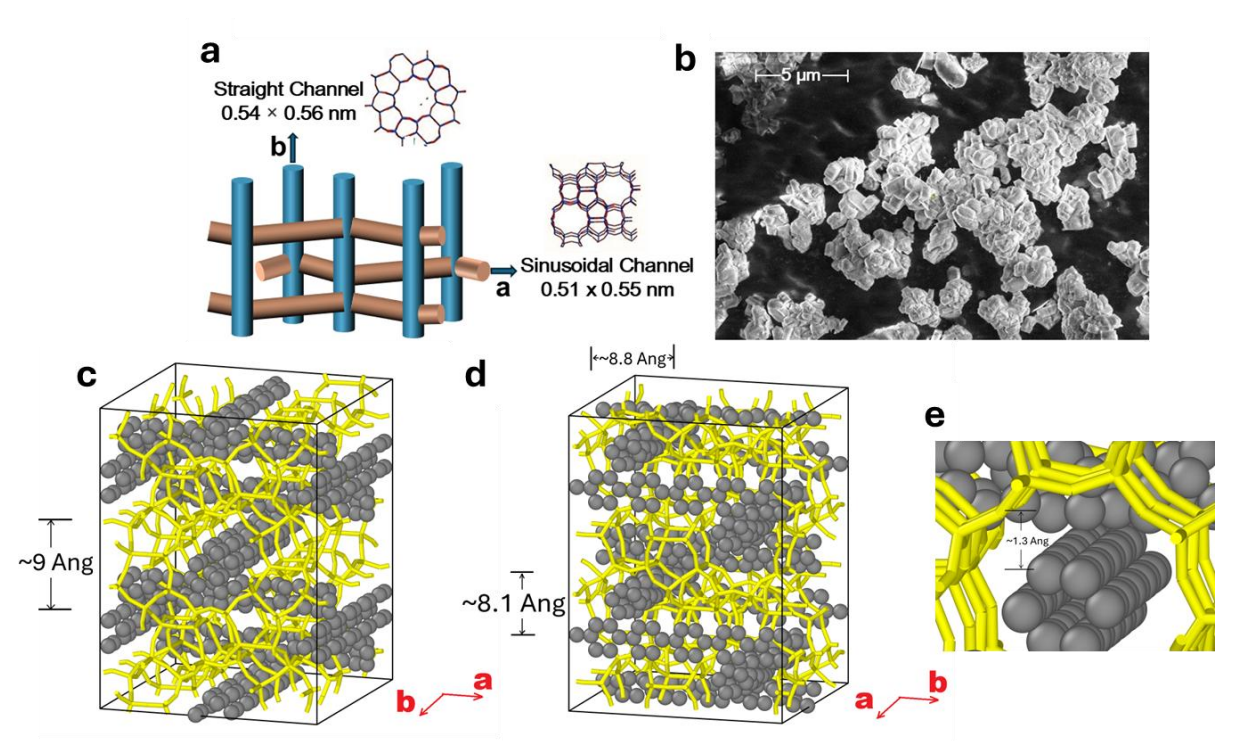


**Figure 5** | **Crystalline structure of CNT@ZSM-5. a**, A schematic picture of the pore structure of ZSM-5. **b**, SEM image of the ZSM-5 zeolite crystallites of typical size of 3 to 4 micrometers, which serve as the template for growing boron-doped networks of carbon nanotubes inside their pores, forming CNT@ZSM-5. **c**, **d**, Illustration of the crystalline structure of the ZSM-5 zeolite, depicted by the skeletal framework for visual clarity, with its pored filled with a 3D network of (2,1) CNTs in the channels along the a axis, and (3,0) CNTs in the channels along the b axis. **e**, Details of the region where perpendicular nanotubes are separated by a small spatial gap of only 1.3 Angstroms. While at such a small separation some bonding may be inevitable, such spots would remain the mechanically weak points in the system, thereby accounting for the large pressure dependence of the  $T_c$  arising from 1D to 3D crossover.

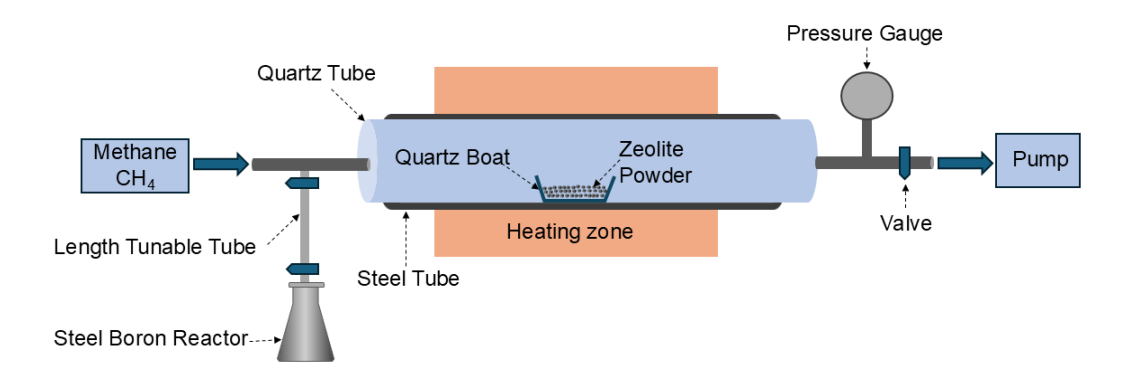


Figure 6 | Chemical vapour deposition and boron-doping setup for the fabrication of doped carbon nanotube networks in ZSM-5.

In Fig. 7a we show Raman spectroscopy data (Jobin Yvon T64000, 514 nm laser excitation) which reveals two prominent Raman peaks: the  $G^+$  band (1586 cm<sup>-1</sup>) and  $G^-$  band (1345 cm<sup>-1</sup>). Whereas the  $G^+$  mode is indicative of relative C-C vibration of the  $\sigma$  bond along the axial direction, the  $G^-$  mode configuration is indicative of the strong  $\sigma\pi$  bond mixing in the (2,1) and hence exhibits a value close to diamond's G band frequency of 1332 cm<sup>-1</sup>. In the present case the  $G^+$  band matches reasonably well with the ab-initio calculated value of 1540 cm<sup>-1</sup> for the

(3,0) CNT. The G<sup>-</sup> band matches well with the ab-initio calculated value of 1363 cm<sup>-1</sup> for the (2,1) CNTs.

The above identification of the two types of CNTs is further reinforced by the existence of two sets of pore channels in ZSM-5, with differing cross section dimensions (see Fig. 5a). Whereas (3,0) CNTs can fit into the channels along the b axis, only (2,1) CNTs can fit into the channels along the a axis owing to its slightly elliptical cross-sectional shape with a smaller minor axis.

Ab-initio calculations also revealed the phonon spectrum of (2,1) CNT to exhibit imaginary frequencies at almost all the wavenumbers, indicating instability and hence requiring the confinement of the channel walls for its stability.

The calculated Raman radial breathing mode (RBM) frequency is 813 cm<sup>-1</sup> for the (3,0), which agrees reasonably well with the small Raman peak at 843 cm<sup>-1</sup>. For (2,1), however, the calculated Raman frequency is only 699 cm<sup>-1</sup> owing to its instability tendency, as shown in Extended Data Fig. 11. The stability of the (2,1) CNTs is maintained by the confinement pressure of the channel wall. Since the confinement pressure is unknown, the accurate identification of the (2,1) RBM frequency remains unidentified at present. Details of the abinitio calculations and the relevant electron band-structures and phonon spectra can be found in the section on supporting ab-initio calculation.

Fig. 7b shows the result of the thermogravimetric analysis (Q5000 (TA)) (TGA), which quantified the carbon content to be 27.9 wt%, corresponding to a 94% pore-filling ratio.

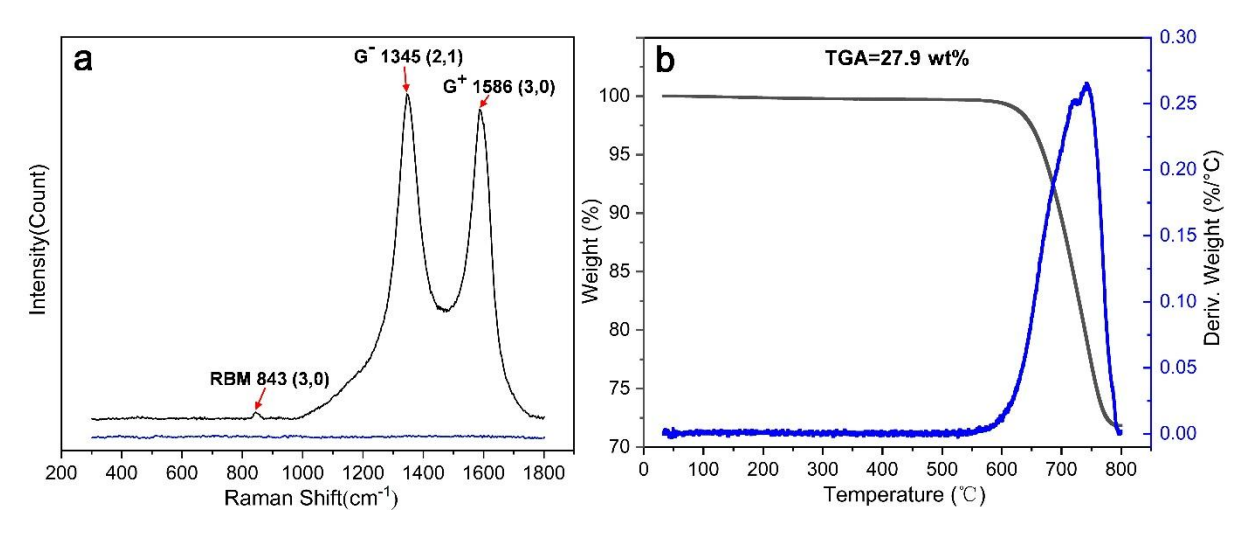


Figure 7 | Characterization of boron-doped carbon networks in ZSM-5: a, Raman spectrum showing two sharp G band peaks, the  $G^+$  for (3,0) at 1586 cm<sup>-1</sup>, and  $G^-$  for (2,1) at 1345 cm<sup>-1</sup>. Ab-initio calculated values are 1540 cm<sup>-1</sup> for (3,0), and 1363 cm<sup>-1</sup> for (2,1). The latter signifies the strong  $\sigma\pi$  bond mixing in (2,1) and hence close to that of diamond (sp3) at 1332 cm<sup>-1</sup>. For the RBM frequencies, the ab-initio value is 813 cm<sup>-1</sup> for (3,0), in reasonable agreement with the small observed 843 Raman peak. However, for (2,1) CNTs since the ab-initio results on the phonon spectrum clearly indicate instability (see Extended Data Fig. 11), the channel wall confinement pressure is necessary to maintain stability. As the confinement pressure is unknown, its RBM frequency cannot be identified. **b**, Thermogravimetric analysis (TGA) diagram that shows a two-peak structure in the differential (blue) curve. The TGA loss curve (black) shows a total of 27.9 wt% of carbon, corresponding to 94% pore occupation ratio.

We used Energy-dispersive X-ray spectroscopy (EDS) (JSM-IT800) to estimate the level of boron incorporation. The resulted showed a carbon concentration of  $45.08\pm0.08$  wt% and boron concentration of  $4.72\pm0.13$  wt%. By taking the atomic weight of boron to be 10.81 and that of

carbon to be 12.01, we obtain the concentration of boron in doped carbon to be  $10.42\pm0.26$  at%. Rounding off to whole numbers to facilitate the ab-initio calculations, we used C: B ratio as 10:1 for the minimum estimate, and 9:1 for the maximum estimate. The results of doping on the Fermi level are shown in Extended Data Figure 11.

#### **DC** magnetization

DC magnetization was measured with a commercial Quantum Design® Vibrating Sample SQUID magnetometer which allows high relative resolution measurements of  $10^{-9}-10^{-8}$  emu. Temperature dependent data was taken under zero-field cooled (ZFC) and field cooled (FC) conditions upon stabilizing the temperature with averaging times of 2-10 seconds. The sample was attached to the sample holder using highly diluted Model VGE7031 insulating varnish/adhesive (LakeShore Cryotronics®). The glue has slightly paramagnetic properties, which can be minimized through strong dilution with ethanol. We also attempted using different types of vacuum grease, which showed a smaller almost temperature independent background contribution, but the transition to a solid phase caused some unwanted anomalies. To manipulate the raw data as little as possible, we used linear background fits in a relatively small temperature interval to remove this background. Raw data is shown in Extended Data Fig. 6 - 8. The background stems partially from a paramagnetic background from the zeolite and glue used to mount the sample, as well as from an unwanted small linear signal drift of the SQUID magnetometer.

# Specific heat

The specific heat was measured with a dedicated home-made alternating temperature (AC) calorimeter with unique design where a sapphire sample chip with Joule heater deposited to its back is suspended on a thermopile made from 8 AuFe0.07% / Chromel thermocouples [35]. The sample temperature was modulated at a frequency of  $\sim$ 1.4 Hz with a temperature modulation kept below 1 mK amplitude. The thermocouple voltage was amplified  $10^4$  times by a Model A20 DC Nanovolt amplifier (EM Electronics®) which is free from 1/f noise and fed into a Model SR830 digital lock-in amplifier (Stanford Research Systems®). The chip is attached to a copper block with additional thermometer, which serves as thermal bath. The calorimeter is enclosed in a sealed vacuum chamber with thermal link to the environment and inserted in a  $^4$ He variable temperature inset of a superconducting magnet cryostat. The addenda of the chip heat capacity was determined separately and removed. The unique design allows for very high relative resolution measurements with  $\Delta C/C$  as small as  $10^{-4}$ . Data was taken at each 1 mK at a cooling rate of 0.1-0.5 K/min with the high datapoint density allowing further signal smoothing by adjacent averaging of datapoints.

#### **Electrical resistance**

The electrical resistance was measured using macroscopic samples consisting of approximately 1 mg of powder. Since the powder lacked sufficient cohesion, we fabricated an insulating polyamide body with a 1.2 mm screw hole drilled completely through its length (Fig. 8a). The powder was filled into the hole and compressed between two screws, forming a conducting sample where the screws served as terminals for a two-probe measurement. In a subsequent iteration, we adopted an improved design featuring two screw holes crossing at a 45-degree angle, allowing the sample to be compressed by four screws serving as terminals for a four-probe experiment (Fig. 8b). Since it turned out that superconductivity in CNT@ZSM-5 shows an extreme sensitivity to the pressure applied by the screws, the two-probe design even allowed a simple pressure study of the superconducting transition, where the pressure was roughly calculated from the measured torque applied to the screws. For the four-probe device we attempted the same (Extended Fig. 5e), but the design caused significant pressure gradients

causing a large broadening of the superconducting transition. We used a Model 6221 AC and DC Current Source (Keithley®) current source in combination with either a digital Stranford Research Systems SR850® lock-in amplifier for AC measurements, or for some measurements an Agilent 34401A® digital multimeter with current reversal technique to avoid thermoelectrical voltages for DC measurements. Both methods resulted in equally good results.

Initially, we used a <sup>4</sup>He cryostat with a variable temperature insert, but we found that the required temperature range extended beyond ambient temperature, which was inaccessible with the low-temperature device. Therefore, we switched to a simpler experimental setup in which the experiment was mounted in a closed, solid copper pot containing an integrated, calibrated Pt1000 thermometer. The copper pot served as a thermal bath. The sample stage was wrapped in adhesive copper tape to establish good thermal contact with the thermometer and the thermal bath. The measurement protocol consisted of first cooling the pot with liquid nitrogen to 77 K, then measuring while the pot was slowly warmed up to ambient temperature. This provided results that were in perfect agreement with those obtained using the cryostat. Subsequently, we used a hot plate to heat the pot up to 400 K at a rate of ~1 K/min.

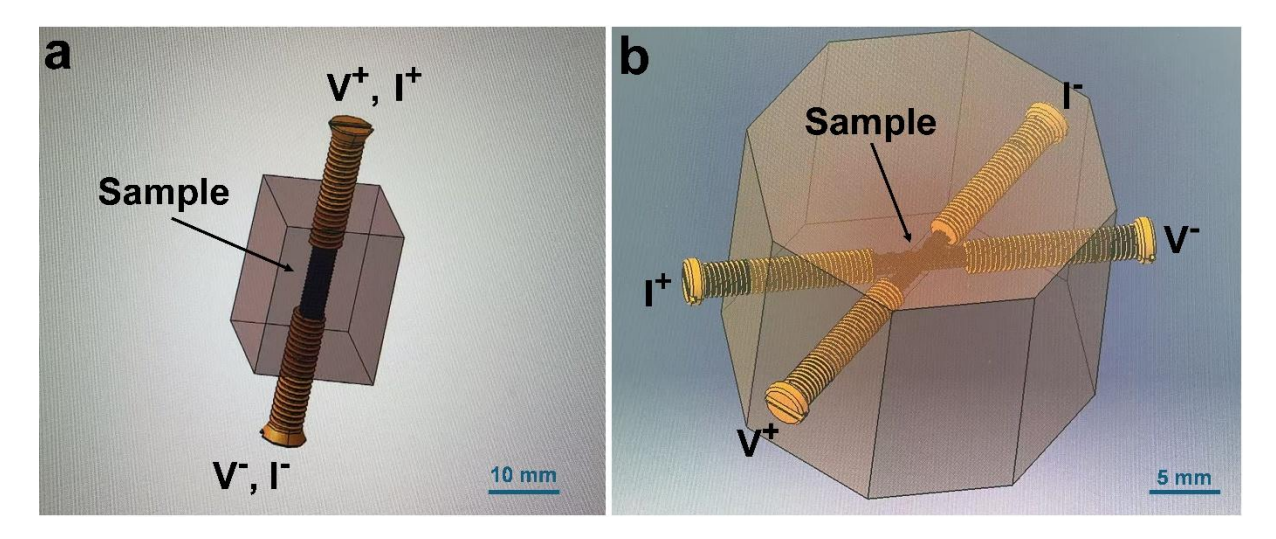


Figure 8 | Screw devices for measurements of the electrical resistance of the powder sample. The sample is placed in the centre of a M1.2 screw holes which traverse through the entire length of a polyamide body and compressed between one pair of screws (a) or two pairs of screws in screw holes intersecting at a 45-degree angle (b). The pairs of screws served at the same time as electrical terminals for either two-probe measurements (a) or four-probe measurements (b). The two-terminal device (a) could at the same time used as a simple pressure cell capable of applying pressure of up to ~0.1 kbar.

#### **Point-contact spectroscopy**

The point contact spectroscopy data was taken using a home-made scanning tunnelling probe. Many CNT@ZSM-5 crystallites were densely packed on a conducting cupper substrate and subsequently covered by a very thin (~5 Angstrom) gold film which serves to supply the electrical contact near the tip rather than passing the current through the crystallites from the back of the substrate. The idea behind the design was to search for a proximity induced superconducting gap via tunnelling spectroscopy in the gold layer, while it turned out that better results were achieved when the tip was pierced through the gold layer to directly contact the CNT@ZSM-5 crystals in point contact mode. Data was taken with different contact resistances between the tip and the CNT@ZSM-5 crystals thus varying the barrier height so that superconductivity can be probed in both, the low-transparency tunnelling limit and the high transparency Andreev limit [33,40], which both provides a distinct response. Note that the

ability to tune the contact through both limits can serve as firm evidence for superconductivity as the observation of Andreev reflection within the bias voltage range of a superconducting gap can only be due to superconductivity.

To carry out the point contact tunnelling and Andreev reflection spectroscopy, we employed a Keithley 6221® source capable of delivering both AC and DC currents, in conjunction with an Agilent 34411A® digital multimeter and an SR830 lock-in amplifier. The measurement protocol involved varying a DC current incrementally in small steps from negative to positive values. This DC sweep established the bias voltage across the junction. Simultaneously, a small-amplitude AC current – comparable in magnitude to the DC step size – was superimposed to enable lock-in detection of the differential conductance, dI/dV, as a function of the applied bias. The digital multimeter was used to monitor the resulting voltage. This current-driven approach is particularly well-suited for probing high to intermediate transparency point-contacts. The measurements were done in a <sup>3</sup>He insert within a 15 T superconducting magnet cryostat which was optimized for vibrational damping required in such experiments.

#### Supporting ab-initio calculations

We employed first-principle density functional theory method to investigate the electronic band structure and the phonon spectrum of (2,1) and (3,0) CNTs. A mixed-basis pseudo-potential code [48,49] is used to perform the calculations. We use plane wave with 24 Ryd cutoff energy and 2s- and 2p-like localized functions to describe the valance electrons of carbon, and the Brillouin zone sampling in the band structure and phonon spectrum calculations are set to  $1\times1\times72$  k-points for (2,1) CNT and  $1\times1\times256$  k-points for (3,0) CNT, respectively. The atomic structures are fully relaxed before the band structure and phonon spectrum calculations. The results can be found in Extended Data Fig. 11. The results show the (2,1) CNT and (3,0) CNT to be metallic, and boron doping moves down the Fermi level of (2,1) CNT to the vicinity of the van-Hove singularity. This is favorable to introduce electron-phonon interaction related phenomena, like phonon mediated superconductivity and Peierls distortion. As the CNTs are embedded in a three-dimensional network, Peierls distortion is suppressed. We deduce that boron doping is likely to introduce superconductivity in our case. Phonon spectra show that individual (3,0) is robust against Peierls distortion, while individual (2,1) CNT is unstable. Phonon frequency softening due to electron-phonon coupling can be clearly observed in the phonon spectrum of (3,0) CNT.

Note that the confinement of the zeolite framework is not considered in this ab-initio calculation, because such a system is beyond our computational capacity. However, the confinement of the zeolite framework is very important to stabilize the (2,1) CNTs and therefore plays a crucial role in the emergence of superconductivity. Also, it should be noted that the phonon spectra of both types of CNTs are calculated for the undoped case. The electron-phonon coupling would scatter electrons around the Fermi level, so the variation of the Fermi level is crucial to the phonon spectrum and consequently the total phonon mediated electron-electron interaction. These questions remain to be investigated in the future.

#### Data availability

The data that support the findings of this study are available at [to be added].

#### Code availability

The code that supports the findings of this study is available from the corresponding authors upon reasonable request.

#### References

- [1] Onnes, H. K. The Resistance of Pure Mercury at Helium Temperatures (Springer, Dordrecht, 1911).
- [2] Hepting, M. Nickelates join the club of high-temperature superconductors. Nature **62**, 475-476 (2023).
- [3] Bardeen, J., Cooper, L.N., Schrieffer, J.R. Theory of Superconductivity, Phys. Rev., 108, 1175-1204 (1957).
- [4] McMillan, W. L.: Phys. Rev. 167, 331-344 (1968).
- [5] Bednorz, J. G. & Müller, K. A. Possible high-T<sub>c</sub> superconductivity in the Ba–La–Cu–O system, Zeitschrift für Physik B Condensed Matter **64**, 189 (1986).
- [6] Wu, M. K., Ashburn, J. R., Torng, C. J., Hor, P. H., Meng, R. L., Gao, L., Huang, Z. J., Wang, Y. Q. & Chu, C. W., Superconductivity at 93 K in a new mixed-phase Y-Ba-Cu-O compound system at ambient pressure, Phys. Rev. Lett. **58**, 908 (1987).
- [7] Schilling, A., Cantoni, M., Guo, J. D. & Ott, H. R. Superconductivity above 130 K in the Hg–Ba–Ca– Cu–O system, Nature **363**, 56 (1993).
- [8] For a recent review see e.g. Tranquada, J. M., Dean, M. P. M., Q. Li, Q. Superconductivity from Charge Order in Cuprates, J. Phys. Soc. Jpn. **90**, 111002 (2021).
- [9] Takahashi, H., Igawa, K., Arii, K., Kamihara, Y., Hirano, M., Hosono, H. Nature **453**, 376–387 (2008).
- [10] Ren, Z. A., Lu, W., Yang, J., Yi, W., Shen, X. L., Li, Z. C., Che, G. C., Dong, X. L., Sun, L. L., Zhou, F., Zhao, Z.X. Chin. Phys. Lett. **25**, 2215–2216 (2008).
- [11] Ge, J. F., Liu, Z. L., Liu, C. et al. Superconductivity above 100 K in single-layer FeSe films on doped SrTiO3. Nature Mater 14, 285–289 (2015).
- [12] Wang, B. Y., Lee, K., Goodge, B. H., Experimental Progress in Superconducting Nickelates, Annu. Rev. Condens. Matter Phys. 15, 305-324 (2024).
- [13] Sun, H., Huo, M., Hu, X. et al. Signatures of superconductivity near 80 K in a nickelate under high pressure. Nature **621**, 493–498 (2023).
- [14] Zhou, G., Lv, W., Wang, H. et al. Ambient-pressure superconductivity onset above 40 K in (La,Pr)<sub>3</sub>Ni<sub>2</sub>O<sub>7</sub> films. Nature **640**, 641–646 (2025).
- [15] Ashcroft, N. W., Metallic Hydrogen: A High-Temperature Superconductor? Phys. Rev. Lett., **21**, 1748-1749 (1968).
- [16] Zhang, S., Zhang, M. & Liu, H. Superconductive hydrogen-rich compounds under high pressure. Appl. Phys. A **127**, 684 (2021).
- [17] Drozdov, A. P., Eremets, M. I., Troyan, I. A., Ksenofontov V., Shylin, S. I., Nature **525**, 73–76 (2015).
- [18] Drozdov, A. P., Kong, P. P., Minkov, V. S., Besedin, S. P., Kuzovnikov, M. A., Mozaffari, S., Balicas, L., Balakirev, F. F., Graf, D. E., Prakapenka, V. B., Greenberg, E., Knyazev, D. A., Tkacz, M., Eremets, M. I., Nature **569**, 528–531 (2019).
- [19] Garisto, D. Exclusive: official investigation reveals how superconductivity physicist faked blockbuster results, Nature **628** (2024), pp. 481-483.
- [20] Iijima, S., Helical microtubules of graphitic carbon. Nature **354**, 56-58 (1991).
- [21] Oberlin, A, Endo, M, Koyama, T. Filamentous growth of carbon through benzene decomposition. Journal of Crystal Growth **32**, 335-349 (1976).
- [22] Benedict, L. X., Crespi, V. H., Louie, S. G., Cohen, M. L. Static conductivity and superconductivity of carbon nanotubes: Relations between tubes and sheets. *Physical* Review B. **52**, 14935 (1995).
- [23] Hebard, A., Rosseinsky, M., Haddon, R. et al. Superconductivity at 18 K in potassium-doped C60. Nature **350**, 600–601 (1991).

- [24] Tang, Z. K., Zhang, L. Y., Wang, N., Zhang, X. X., Wen, G. H., Li, G. D., Wang, J. N., Chan, C. T. & Sheng, P. Science **292**, 2462 (2001).
- [25] Lortz, R., Zhang, Q., Shi, W., Ye, J., Qiu, C., Wang, Z., He, H., Sheng, P., Qian, T., Tang, Z. K., Wang, N., Zhang, X. X., Wang, J. & Chan, C. T. Proc. Natl. Acad. Sci. USA 106, 7299 (2009).
- [26] Ieong, C., Wang, Z., Shi, W., Wang, Y., Wang, N., Tang, Z. K., Sheng, P. & Lortz, R. Observation of the Meissner state in superconducting arrays of 4-Å carbon nanotubes, Phys. Rev. B **83** (2011).
- [27] Wang, Z., Shi, W., Xie, H., Zhang, T., Wang, N., Tang, Z., Zhang, X., Lortz, R., Sheng, P., Sheikin, I. & Demuer, A. Superconducting resistive transition in coupled arrays of 4Å carbon nanotubes, Phys. Rev. B **81**, 174530 (2010).
- [28] Zhang, B., Liu, Y., Chen, Q., Lai, Z.& Sheng, P., Observation of high Tc one dimensional superconductivity in 4 angstrom carbon nanotube arrays, AIP Advances 7, 025305 (2017).
- [29] Pan, J., Zhang, B., Hou, Y., Zhang, T., Deng, X., Wang, Y., Wang, N., Sheng, P. Superconductivity in boron-doped carbon nanotube networks, arXiv:2303.15980.
- [30] Shi, W., Wang, Z., Zhang, Q. et al. Superconductivity in Bundles of Double-Wall Carbon Nanotubes. Sci Rep 2, 625 (2012).
- [31] Cao, Y., Fatemi, V., Fang, S. et al. Unconventional superconductivity in magic-angle graphene superlattices. Nature **556**, 43–50 (2018).
- [32] Núñez-Regueiro, M., Devillers. T., Beaugnon. E., de Marles. A., Crozes. T., Pairis. S., Swale. C., Klein. H., Leynaud. O., Hadj-Azzem. A., Gay. F., Dufeu. D. Magnetic field sorting of superconducting graphite particles with T<sub>c</sub>>400K, arXiv:2410.18020.
- [33] Daghero, D. & Gonnelli, R. S. Supercond. Sci. Technol. 23, 043001 (2010).
- [34] Kokotailo, G., Lawton, S., Olson, D., et al. Structure of synthetic zeolite ZSM-5 [J]. Nature 272, 437-438 (1978).
- [35] Lortz, R., Lin, F., Musolino, N., Wang, Y., Junod, A., Rosenstein, B. & Toyota, N. Thermal fluctuations and vortex melting in the Nb<sub>3</sub>Sn superconductor from high resolution specific heat measurements, Phys. Rev. B **74**, 104502 (2006).
- [36] Pasler, V., Schweiss, P., Meingast, C., Obst, B., Wühl. H., Rykov, A. I., Tajima, S. 3*D–XY* Critical Fluctuations of the Thermal Expansivity in Detwinned YBa<sub>2</sub>Cu<sub>3</sub>O<sub>7-δ</sub> Single Crystals Near Optimal Doping. Phys. Rev. Lett. **81**, 1094 (1998).
- [37] Meingast, C., Pasler, V., Nagel, P., Rykov, A., Tajima, S. & Olsson, P. Phase Fluctuations and the Pseudogap in YBa<sub>2</sub>Cu<sub>3</sub>O<sub>x</sub>, Phys. Rev. Lett. **86** (2001).
- [38] Lortz, R., Meingast, C., Rykov, A. I., Tajima, S. Magnetic-field-induced finite-size effect in the nigh-temperature superconductor YBa<sub>2</sub>Cu<sub>3</sub>O<sub>7-delta</sub>: a comparison with rotating superfluid <sup>4</sup>He. Phys Rev Lett. **91**, 207001 (2003).
- [39] Schilling, A., Fisher, R. A., Phillips, N. E., Welp, U., Kwok, W. K., Crabtree, G. W. Anisotropic Latent Heat of Vortex-Lattice Melting in Untwinned YBa<sub>2</sub>Cu<sub>3</sub>O<sub>7-d</sub>, Phys. Rev. Lett. 78, 4833 (1997).
- [40] Blonder, E., Tinkham, M., & Klapwijk, T. M. Transition from Metallic to Tunneling Regimes in Superconducting Microconstrictions: Excess Current, Charge Imbalance, and Supercurrent Conversion. Phys. Rev. B 25, 4515 (1982).
- [41] Wang, Y., Plackowski. T., Junod, A., Specific heat in the superconducting and normal state (2–300 K, 0–16 T), and magnetic susceptibility of the 38 K superconductor MgB<sub>2</sub>: evidence for a multicomponent gap, Physica C **355**, 179-193 (2001).
- [42] Kostić, P., Veal, B., Paulikas, A. P., Welp, U., Todt, V. R., Gu, C., Geiser, U., Williams, J. M., Carlson K. D. et al. Paramagnetic Meissner effect in Nb, Phys. Rev. B **53**, 791 (1996).
- [43] Nguyen, A. K., Sudbø, A. Topological phase fluctuations, amplitude fluctuations, and criticality in extreme type-II superconductors, Phys. Rev. B **60**, 15307 (1999).

- [44] Tešanović, Z. Extreme type-II superconductors in a magnetic field: A theory of critical fluctuations, Phys. Rev. B **59**, 6449 (1999).
- [45] Wang, Y., Li, L., Ong, N. P. Nernst effect in high-*Tc* superconductors, Phys. Rev. B **73**, 024510 (2006).
- [46] Eagles, D. M. Possible pairing without superconductivity at low carrier concentrations in bulk and thin-film superconducting semiconductors. Phys. Rev. **186**, 456 (1969).
- [47] Božović, I., Levy, J. Pre-formed Cooper pairs in copper oxides and LaAlO<sub>3</sub> SrTiO<sub>3</sub> heterostructures. *Nat. Phys.* **16**, 712–717 (2020).
- [48] Meyer. B, Elsaesser. C and Faehnle. M, FORTRAN90 Program for Mixed-Basis Pseudopotential Calculations for Crystals, Max-Planck-Institut for Metallforschung, Stuttgart (unpublished).
- [49] Heid. R and Bohnen. K. P, Linear response in a density-functional mixed-basis approach. *Phys. Rev. B.* **60**, R3709 (1999).

#### **Author contributions**

PS sustained the endeavour on carbon nanotube superconductivity for the past 25 years; he proposed the in-situ boron doping approach, provided guidance on the fabrication of samples that lead to the present results, and coordinated the whole effort. NW and PS initiated the present investigation. YW, THK, RH, YHN, TTL and TZ contributed equally to this work and share first authorship. YW, RH, and WMC fabricated the samples. YH and JP implemented the initial boron doping setup. NW improved upon the boron doping setup and procedure. YW and RL did the magnetization measurements. YW carried out sample characterizations. NW proposed the 2-probe macroscopic measurements of electrical transport, refined by YW and RL in form of a 4-probe set-up. RL, YHN and YW did the transport measurements. RL investigated the pressure dependence, TTL, YHN and RL did the specific heat measurements, THK and RL did the point contact spectroscopy measurements. RL analysed all the experimental data providing evidence for superconductivity. TZ performed ab-initio calculations. PS interpreted the Raman spectrum based on the results of ab-initio calculations. RL wrote the first draft of the manuscript, with contributions from PS and YW.

#### Acknowledgements

We thank U. Lampe for technical support. PS would like to acknowledge and thank the Shun Hing Education and Charity Fund, especially the late Dr. William Mong, for sustained support over two decades. RL thanks K. T. Law for fruitful discussions on the particle hole symmetry of point contact spectra.

#### **Corresponding author**

Correspondence to rolf.lortz@lncmi.cnrs.fr; phwang@ust.hk; sheng@ust.hk

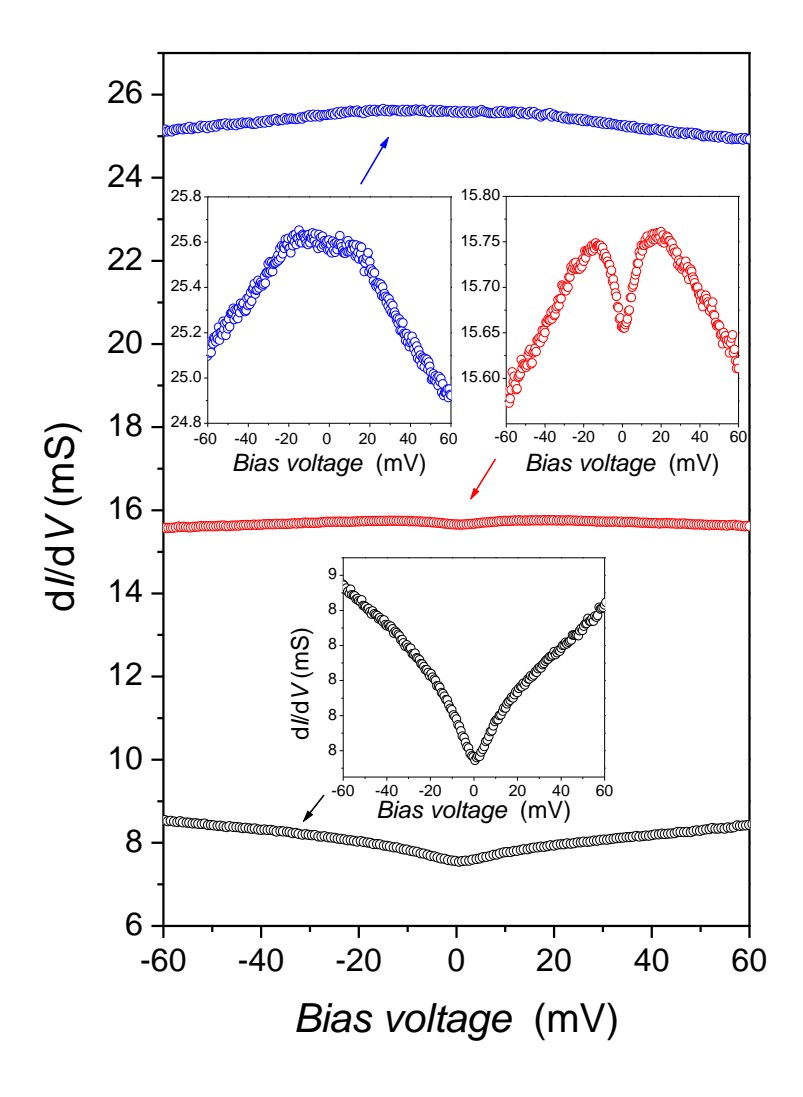
#### **Ethics declarations**

Competing interests

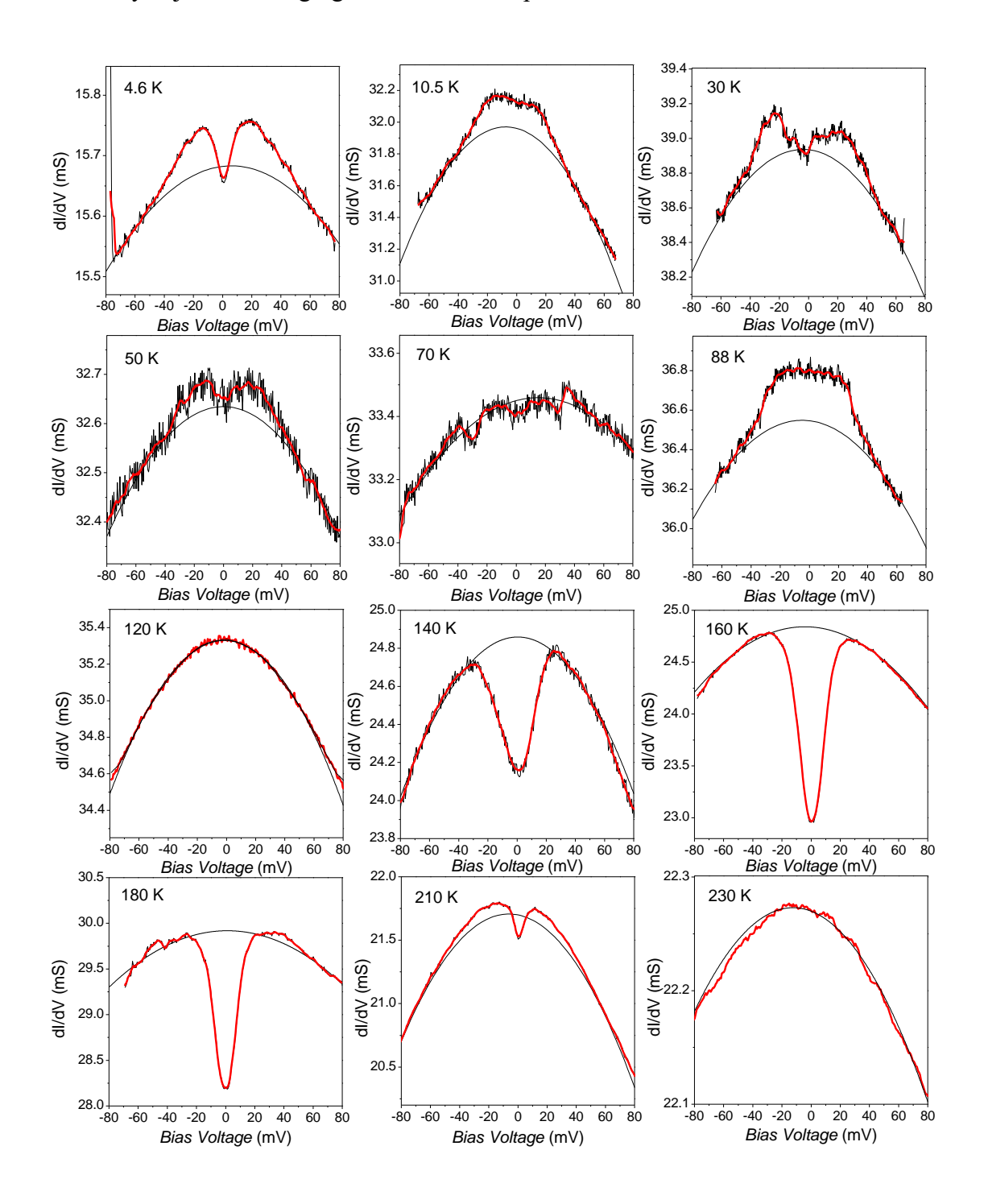
The authors declare no competing interests.

# **Extended data figures**

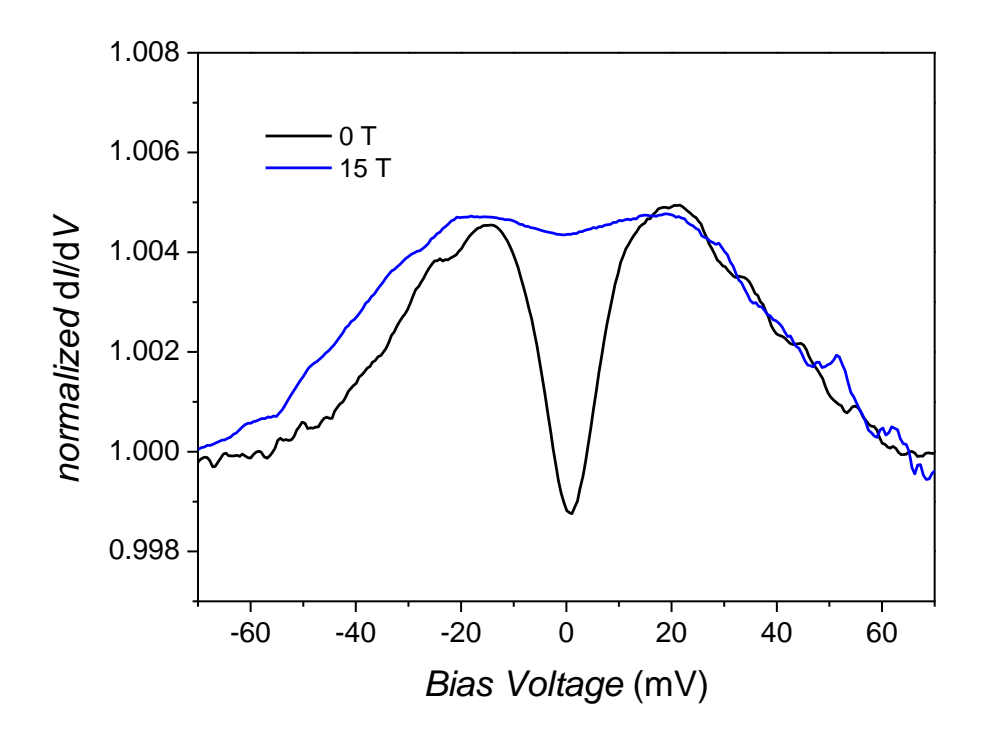
**Extended Data Fig. 1. Point contact spectroscopy on CNT@ZSM-5.** Examples of 3 different point contact spectra taken below 10 K with contact transparencies varying from the low transparency tunnelling limit (black) over an intermediate range (red) to the high transparency Andreev limit (blue). The insets show enlargements of the 3 spectra. The difference was achieved by varying the tip distance from the sample surface. The ability to tune the spectra between these two limits supports a superconducting origin of the spectra.



Extended Data Fig. 2. Selection of raw point contact data at various temperatures with fits of the parabolic background contribution. Black line are the raw data; red lines are data smoothed by adjacent averaging over 5-10 data points.

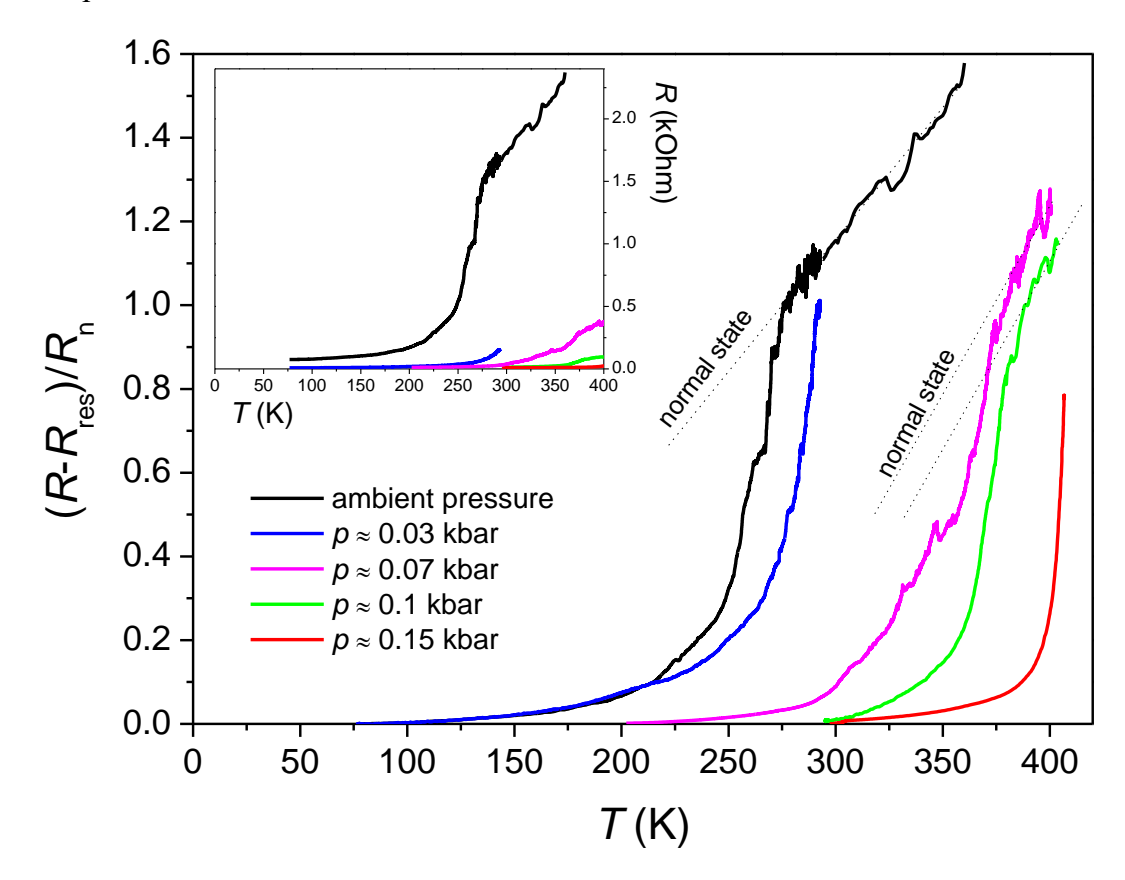


Extended Data Fig. 3. Magnetic field dependence of the point contact spectra of CNT@ZSM-5 taken at 4.6 K. Within the limits of experimental uncertainty, no variation in the superconducting gap is observed, suggesting an exceptionally high upper critical field, likely exceeding 100 T. The apparent asymmetry in the 0 T data is an experimental artifact, attributed to minor tip-position drifts.



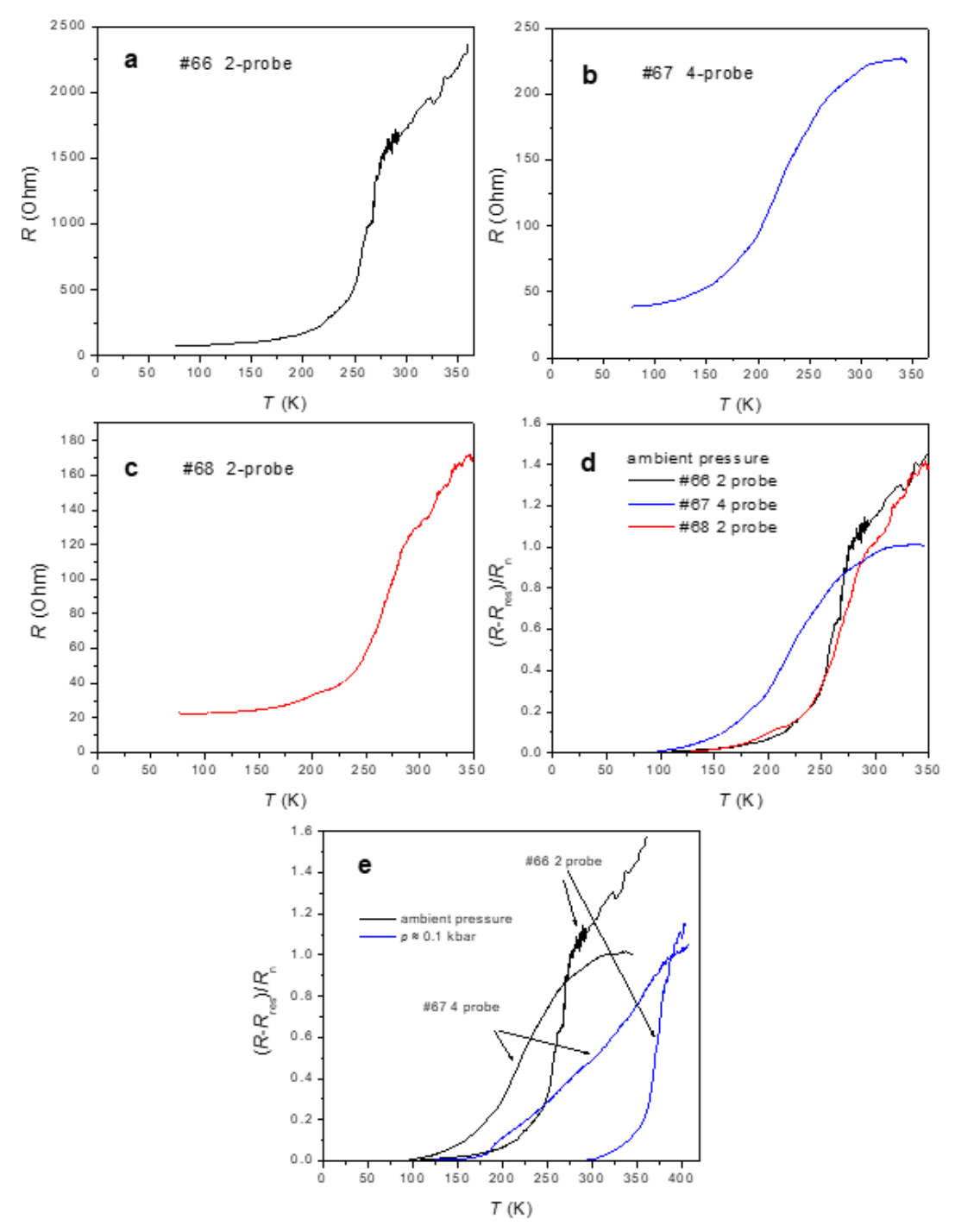
# Extended Data Fig. 4. Supplementary 2 probe pressure dependent resistance data.

Plot of the normalized electric resistivity of batch #66 measured with the 2-probe device similar to Fig. 3, but with additional data taken under different pressures. Note that the pressure values are indicative and estimated from the torque applied to the screws. The normalization of the 0.15 kbar data is approximative, as we were unable to reach the normal state above 400 K with our set-up.

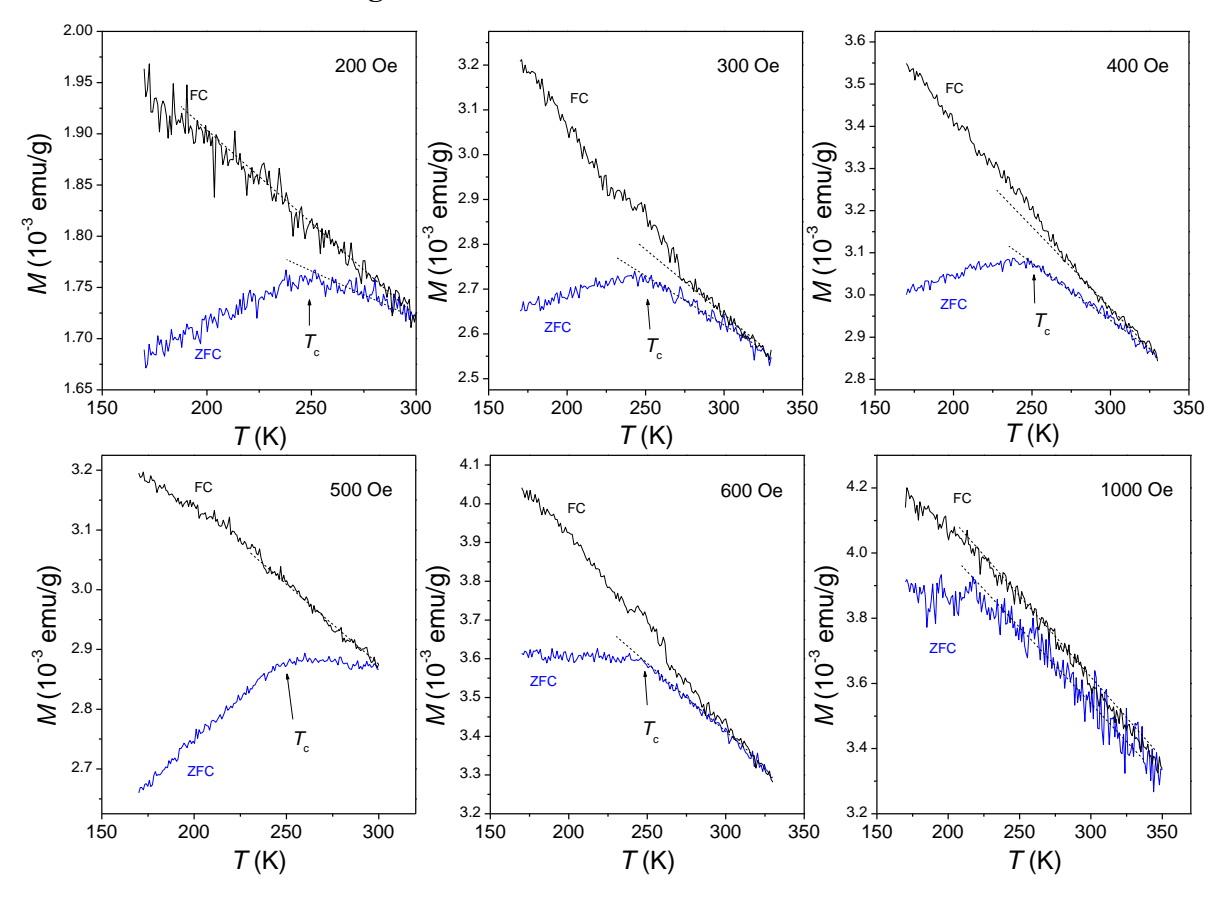


#### Extended Data Fig. 5.a.b.c.d.e. Supplementary resistance data.

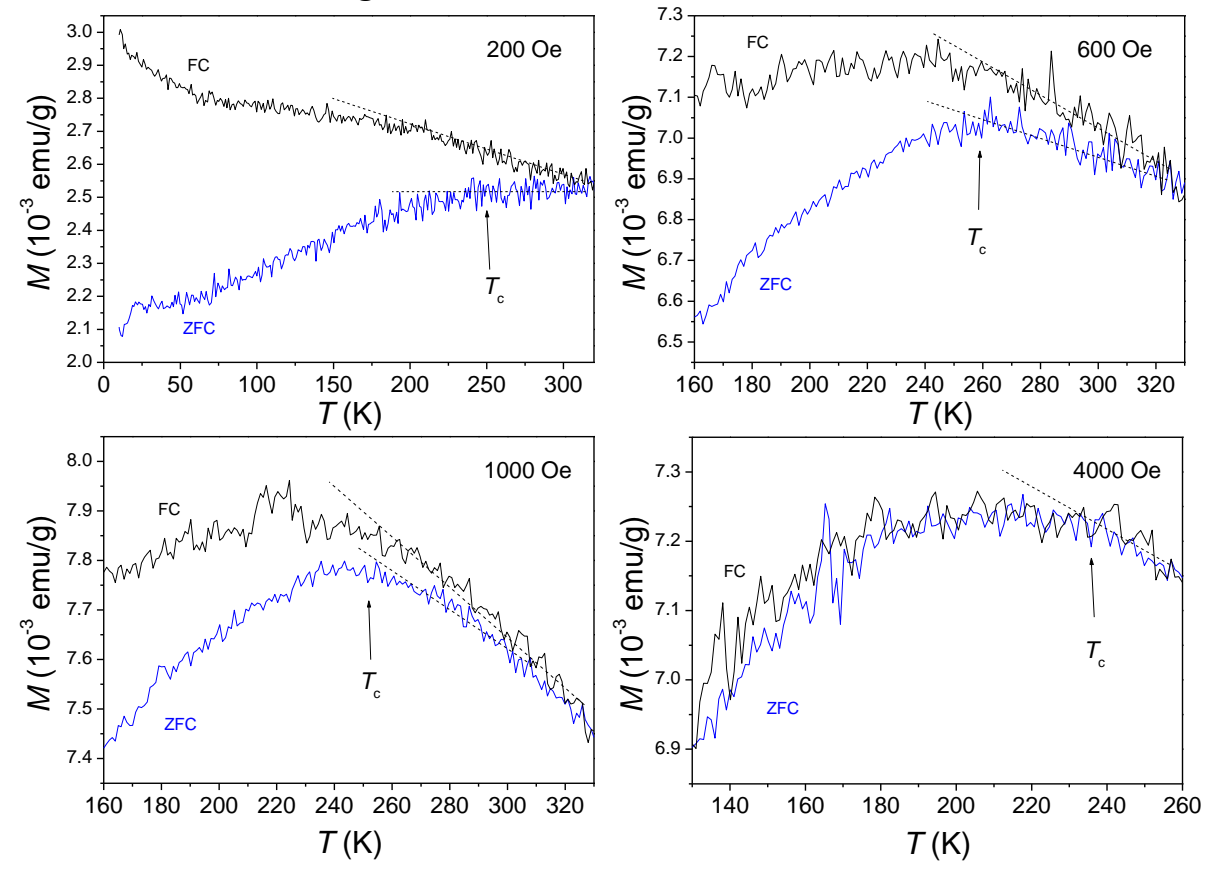
Ambient pressure resistance raw data of batch #67 (a, 2 probe), #68 (b, 4 probe) and #68 (c, 2 probe). d Comparison of normalized ambient pressure resistance data with residual resistance removed of batches #67, #67 and#68. e Normalized resistance data with residual resistance removed measured for #67 with the 4-probe device at zero pressure and ~0.1 kbar in comparison to the 2-probe data from batch #66 shown in the main article. Note that the different width of the ambient pressure transition likely is likely caused by disorder in batch #67 and not due to the 4-probe technique. The large width the #67 pressure data indicates a large pressure gradient in the 4-probe device, making it unsuitable for pressure experiments.



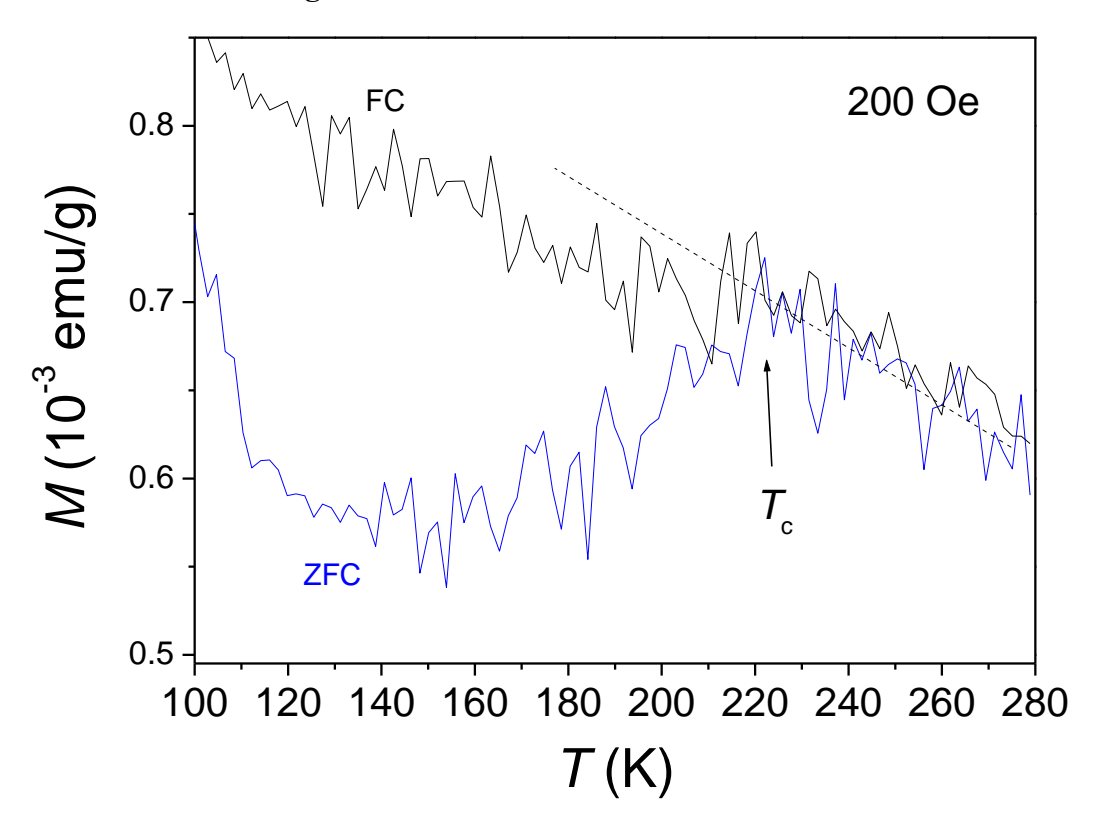
# Extended Data Fig. 6. Selected raw data of the DC magnetization of batch #61 before removal of the linear background.



Extended Data Fig. 7. Selected raw data of the DC magnetization of batch #62 before removal of the linear background.

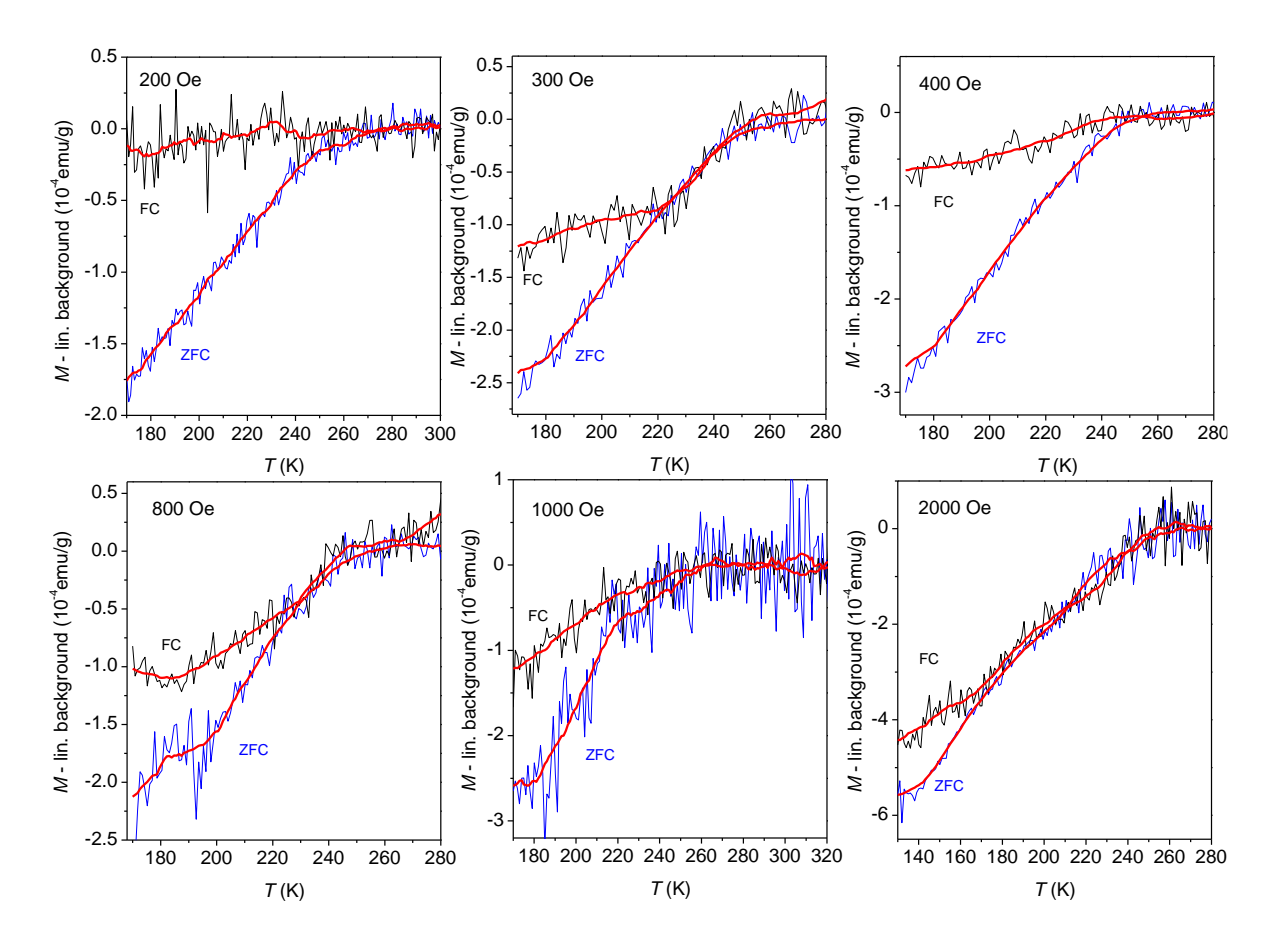


Extended Data Fig. 8. Raw data of the 200 Oe DC magnetization of batch #66 before removal of the linear background.



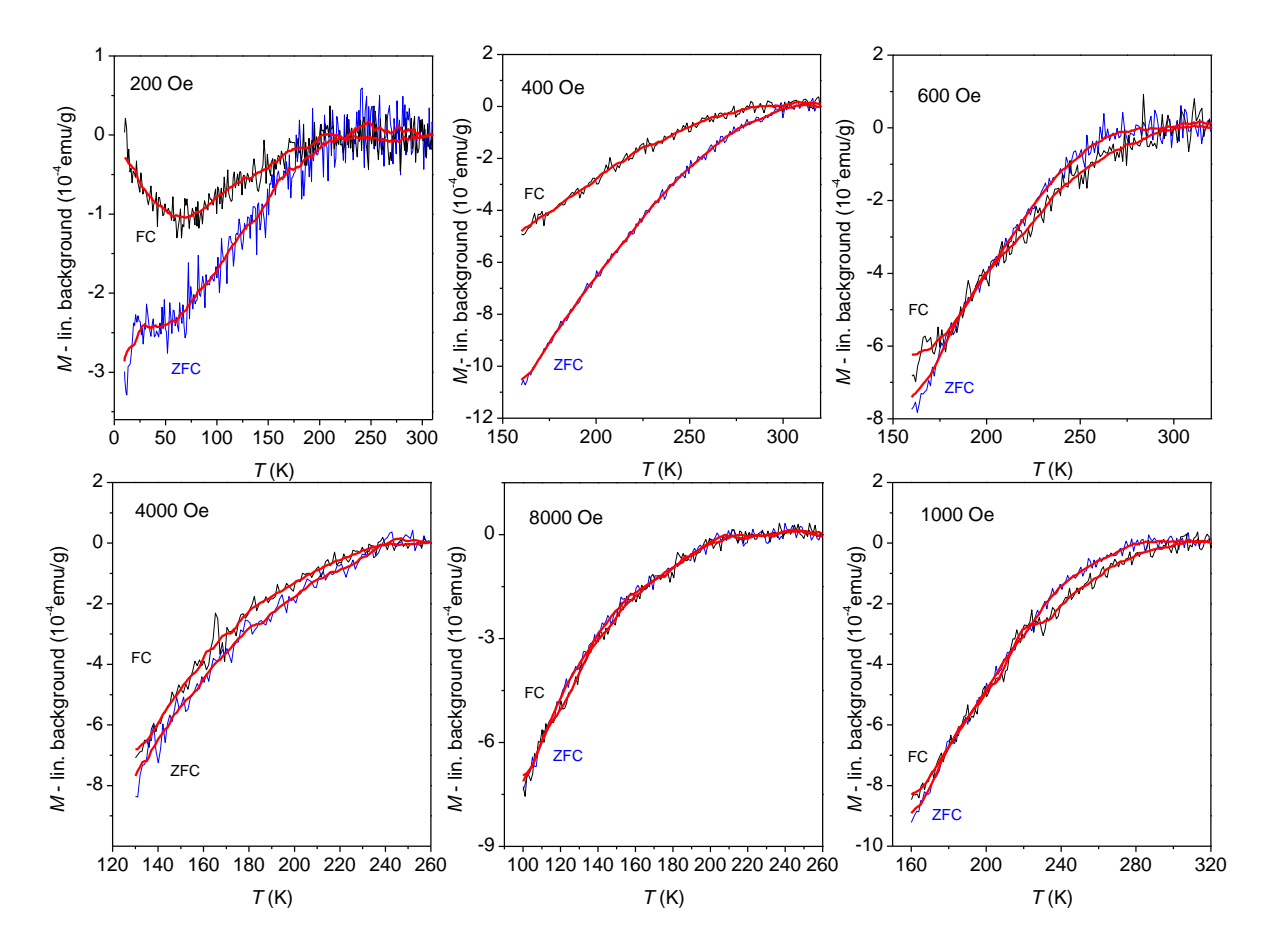
## Extended Data Fig. 9. Supplementary DC magnetization data of batch #61.

Data has been taken under ZFC (blue) and FC (black) conditions in various applied fields. Red lines are data smoothed by adjacent averaging over 5 - 10 data points.



## Extended Data Fig. 10. Supplementary DC magnetization data of batch #62.

Data has been taken under ZFC (blue) and FC (black) conditions in various applied fields. Red lines are data smoothed by adjacent averaging over 5 - 10 data points.



#### Extended Data Fig. 11. Electronic band structure and phonon spectrum calculations.

**a,** Electronic band structure of the (2,1) CNT. The black solid line denotes the Fermi level in the neutral (undoped) state. The shaded blue region represents the range of Fermi levels observed under boron doping, consistent with experimental doping ratios. Upon doping, the Fermi level shifts toward the van-Hove singularity, located at a flat band near -4.78 meV at k = 0. **b,** Electronic band structure of the (3,0) CNT. Both (2,1) and (3,0) CNTs exhibit metallic behavior, as evidenced by the partially filled bands crossing the Fermi level. **c,** Calculated phonon spectrum of the undoped (2,1) CNT. The zero-frequency line is shown as a solid reference. Imaginary phonon modes (plotted as negative frequencies) indicate dynamic instability of the isolated (2,1) CNT, suggesting that structural stability is maintained only when confined by the channel wall. Due to the presence of imaginary modes, no q-point interpolation was applied. **d,** Phonon spectrum of the undoped (3,0) CNT. Softening of phonon modes at specific nesting wave vectors is observed, indicative of electron-phonon coupling effects.

